Improving the Statistical Representation of Tropical Cyclone In-Storm Sea Surface Temperature Cooling

JOSHUA B. WADLER,[a] JOSEPH J. CIONE,[b] SAMANTHA MICHLOWITZ,[c] BENJAMIN JAIMES DE LA CRUZ,[d] AND LYNN K. SHAY[d]

[a] *Embry-Riddle Aeronautical University, Department of Applied Aviation Sciences, Daytona Beach, Florida*
[b] *NOAA/Atlantic Oceanographic and Meteorological Laboratory/Hurricane Research Division, Miami, Florida*
[c] *National Weather Service Louisville Forecast Office, Louisville, Kentucky*
[d] *University of Miami, Department of Ocean Sciences, Miami, Florida*

(Manuscript received 12 July 2023, in final form 12 February 2024, accepted 27 February 2024)

ABSTRACT: This study uses fixed buoy time series to create an algorithm for sea surface temperature (SST) cooling underneath a tropical cyclone (TC) inner core. To build predictive equations, SST cooling is first related to single variable predictors such as the SST before storm arrival, ocean heat content (OHC), mixed layer depth, sea surface salinity and stratification, storm intensity, storm translation speed, and latitude. Of all the single variable predictors, initial SST before storm arrival explains the greatest amount of variance for the change in SST during storm passage. Using a combination of predictors, we created nonlinear predictive equations for SST cooling. In general, the best predictive equations have four predictors and are built with knowledge about the prestorm ocean structure (e.g., OHC), storm intensity (e.g., minimum sea level pressure), initial SST values before storm arrival, and latitude. The best-performing SST cooling equations are broken up into two ocean regimes: when the ocean heat content is less than 60 kJ cm^{-2} (greater spread in SST cooling values) and when the ocean heat content is greater than 60 kJ cm^{-2} (SST cooling is always less than 2°C), which demonstrates the importance of the prestorm oceanic thermal structure on the in-storm SST value. The new equations are compared to what is currently used in a statistical–dynamical model. Overall, since the ocean providing the latent heat and sensible heat fluxes necessary for TC intensification, the results highlight the importance for consistently obtaining accurate in-storm upper-oceanic thermal structure for accurate TC intensity forecasts.

SIGNIFICANCE STATEMENT: The ocean provides the heat and moisture necessary for tropical cyclone (TC) intensification. Since the heat and moisture transfer depend on the sea surface temperature (SST), we create statistical equations for the prediction of SST underneath the storm. The variables we use combine the initial SST before the storm arrives, the upper-ocean thermal structure, and the strength and translation speed of the storm. The predictive equations for SST are evaluated for how well they improve TC intensity forecasts. The best-performing equations can be used for prediction in operational statistical models, which can aid intensity forecasts.

KEYWORDS: Ocean dynamics; Hurricanes/typhoons; Sea surface temperature; Statistics

1. Introduction

It is well known that the ocean provides the heat and moisture necessary for tropical cyclone (TC) intensification through surface sensible and latent heat fluxes (combined referred to as enthalpy fluxes), (e.g., Malkus and Riehl 1960; Emanuel 1986). Since it is extremely difficult to directly measure the turbulent fluxes in the surface layer of a TC due to the dangers of flying crewed aircraft close to the sea surface, the sensible (Q_s) and latent heat (Q_l) fluxes are often parameterized by the bulk aerodynamic formulas [Eqs. (1) and (2), respectively]:

$$Q_s = \rho_a c_p C_h U_{10}(\mathrm{SST} - T_{10}), \quad (1)$$

$$Q_l = \rho_a L_v C_e U_{10}(q_s - q_{10}), \quad (2)$$

where ρ_a is the density of dry air, $C_h = C_e$ are the exchange coefficients for sensible heat and latent heat fluxes, respectively [values can be derived from Zhang et al. (2008)]; c_p is the specific heat of dry air; L_v is the latent heat of evaporation; T_{10} and SST are the 10-m air and sea surface temperature, respectively; and q_{10} and q_s are the 10-m and sea surface specific humidity, respectively. In Eq. (1), the sensible heat flux is directly proportional to the thermal disequilibrium (ΔT) between the ocean surface and the lower atmosphere. In Eq. (2), the latent heat flux is directly proportional to the moisture disequilibrium (Δq) between the ocean surface and the lower atmosphere, with q_s typically derived from the SST using the Clausius–Clapeyron equation.

Since the SST directly influences the surface enthalpy fluxes, it is an important quantity to accurately predict for in-storm conditions. More broadly, recent work has highlighted the importance of the moisture disequilibrium, for TC intensification because it is the dominant metric for variability in the latent heat fluxes (e.g., Shay and Uhlhorn 2008; Cione 2015; Jaimes et al. 2015; Jaimes de la Cruz et al. 2021). A recent study by Jaimes de la Cruz et al. (2021) highlighted the higher sensitivity of the fluxes to Δq at higher surface wind speeds. That is, as wind speeds increase, changes with Δq cause

Corresponding author: Joshua B. Wadler, wadlerj@erau.edu

DOI: 10.1175/WAF-D-23-0115.1

significantly higher change to the latent heat flux than changes to the wind speed alone (see Fig. 4 in that paper).

It has been known for many decades that an SST cold wake forms underneath and behind a TC (e.g., Suda 1943; Fisher 1958; Leipper 1967; Shay et al. 1992; Cione and Uhlhorn 2003; D'Asaro et al. 2007; Mrvaljevic et al. 2013). In most cases, the cold wake is due to upwelling and entrainment of cold subsurface waters driven by horizontal divergence of surface currents as well as instantaneous wind stirring and shear-induced mixing by wind-driven currents (e.g., Hidaka and Akiba 1955; Elsberry et al. 1976; Price 1981; Shay et al. 1998). SST cooling due to shear-driven mixing can depend on the presence of oceanic eddies (e.g., Shay et al. 2000; Jaimes and Shay 2009, 2010; Lin et al. 2009, 2013) as well as upper-ocean stratification (Price et al. 1994; Chan et al. 2001; Price 2009; Sanford et al. 2007), and areas where strong vertical salinity gradients impede mixing during TC passage (e.g., Wang et al. 2011; Balaguru et al. 2018; Rudzin et al. 2018; Hlywiak and Nolan 2019). In some cases over deep warm oceanic regimes, where entrainment cooling is small (e.g., warm eddies), air–sea enthalpy fluxes can cause most of the sea surface cooling (Jaimes et al. 2015).

While the formation of a SST cold wake has received significant attention in the literature, and the upper-ocean processes in TC conditions are understood, the SST evolution directly underneath the storm is less studied. Cione and Uhlhorn (2003) used buoy time series from 23 TCs to show that the magnitude of observed in-storm SST cooling is related to TC intensification, and that errors in inner-core SSTs on order of 1°C can lead to errors in the enthalpy fluxes of over 40%. Nevertheless, predicting the in-storm SST remains a challenge for coupled models, which necessitates increased targeted ocean observations (e.g., Chen et al. 2017; Mogensen et al. 2017). Using linear theory, Lu et al. (2021) built upon the results from Cione and Uhlhorn (2003) by developing a framework for understanding in-storm SST cooling. Lu et al. concluded that SST cooling underneath a storm is related to the initial depth of the mixed layer, the radius of maximum wind speed and latitude.

While satellite-based infrared radiometers cannot obtain SST observations under heavily cloudy conditions, microwave radiometers can penetrate the clouds to observe SST. However, their signals can be attenuated by rainy in-storm conditions. Thus, satellite-based SST products have known limitations under either cloudy or rainy in-storm conditions, which make their estimates unreliable in resolving upwelling-induced SST cooling in TCs (e.g., Huang et al. 2021). Additionally, the daily time interval of satellite-based SST products is not optimal for TC applications. For decades, the ability to obtain instantaneous targeted in-storm SST measurements (as well as prestorm and poststorm measurements) from crewed aircraft using airborne expendable oceanic profilers (Boyd 1987; Shay et al. 2011) and dropsondes with integrated infrared sensors (IRSondes; Zhang et al. 2017) has existed. It is also possible to measure the upper-ocean thermal structure using long-lasting instruments deployed prior to a storm such as Air-Launched Autonomous Micro Observer (ALAMO) floats (Jayne et al. 2022; Sanabia and Jayne 2020), EM-APEX floats (Sanford et al. 2007, 2011; Shay et al. 2019b), ocean drifters (Goni et al. 2017; Domingues et al. 2019), ocean gliders (Testor et al. 2019; Domingues et al. 2021; Le Hénaff et al. 2021), and Saildrones (Meinig et al. 2019; Miles et al. 2021). However, these instruments do not translate with a TC, so the continuous measurement of SSTs under a moving TC remains elusive.

To supplement the scarcity of in-storm SST measurements, statistical relationships between SST cooling with the prestorm oceanic structure and environmental conditions can be used (e.g., Da et al. 2021). Dare and McBride (2011) and Mei and Pasquero (2013) use gridded analyses to statistically evaluate SST cooling, but did not focus on in-storm conditions. The derived in-storm SST used to guide intensity forecasts in the Statistical Hurricane Intensity Prediction Scheme (SHIPS) database (DeMaria et al. 2005) currently uses a predictive equation based on time series of SST from fixed-location buys that are discussed in Cione and Uhlhorn (2003). This predictive equation of SST is a linear function of a TC's latitude, translation speed, and the prestorm SST (discussed further in section 3). With an expanded database, the goal of this manuscript is to derive new, nonlinear predictive equations for in-storm SST cooling and to document how the new equations change the forecast of SST and predicted intensity change. The remaining manuscript will be organized as follows: section 2 will discuss the data sources used to create the predictive equations. Section 3 will discuss how each environmental and ocean structure variable influences the SST cooling as well as the impact of utilizing nonlinear equations. Section 4 will summarize the results with a discussion about the strengths and limitations of our statistical approach.

2. Data and methodology

a. *Tropical cyclone buoy database*

Time series of SST are obtained from the Tropical Cyclone Buoy Database (TCBD; Cione et al. 2000, 2013; Cione and Uhlhorn 2003; Cione 2015; Wadler et al. 2022). The TCBD contains postprocessed and quality-controlled near-surface in situ measurements from the National Data Buoy Center (NDBC; Gilhousen 1988, 1998) and Coastal-Marine Automated Network (C-MAN) platforms [see Cione et al. (2000) for details regarding quality control]. The platforms are primarily located in the western Atlantic Basin, Gulf of Mexico, and the Caribbean Sea (Fig. 1a). As described in Wadler et al. (2022), buoy observations in the TCBD are recorded in hourly increments, with each measurement linked to environmental data from the SHIPS database and information about TCs from the National Hurricane Center (NHC) Extended Best Track Database (EBT; Demuth et al. 2006).

The TCBD currently contains data between 1978 and 2017. The database identifies all NDBC buoy observations that are south of 35°N latitude and within 555 km of a TC center. Under these criteria, there are 2393 unique time series of SST. Since the goal of this study is to document the SST evolution near the inner core of a TC, we constrain the closest physical distance between the TC center and buoy observation

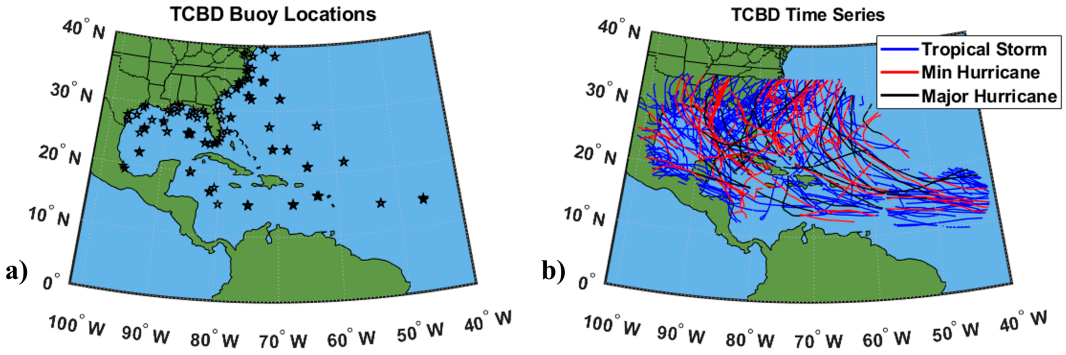

FIG. 1. A geographical map of (a) buoy locations (black stars) and (b) storm tracks from the TCBD that were used in this study. In (b), the tracks are color coded on the basis of maximum TC intensity.

to a maximum of 75 km. This constraint reduces the number of time series to 331 and is implemented as a balance between capturing the SST cooling directly in the core of the TC with increasing the representative sample size. The storm tracks that meet the distance criteria are shown in Fig. 1b. Other physical distances were tested such as data within 50 and 100 km of a TC center, which have 207 and 472 time series, respectively. Of note, we considered constraining distance between the buoy and TC center by a storm size parameter such as within 1.5 times the radius of maximum wind speed (RMW). Except for storms with a small reported RMW (10.1% of the 331 cases where the storm center was within 75 km of a buoy had a reported RMW of 25 km or smaller), a maximum cutoff distance of 1.5 × RMW generally encompasses the same TC inner-core region as the 75-km cutoff distances. In only 2.7% of cases, the RMW is greater than 200 km which makes the 75-km cutoff more limiting to essentially include only the storm center. Using the 1.5 × RMW cutoff as a sensitivity analysis led to slightly reduced correlations between SST cooling and the individual predictors, as compared to the 75-km cutoff analysis used in this manuscript (not shown). Normalizing by the RMW was not used in the final calculations due to uncertainty with the RMW in the EBT database (Landsea and Franklin 2013; Davis 2018), especially in earlier years of the TCBD.

b. *Ocean structure and SMARTS climatology*

Since the only oceanic metric measured by fixed buoys is the SST, TCBD observations are matched to ocean structure variables in the Systematically Merged Atlantic Regional Temperature and Salinity (SMARTS) Climatology (Meyers et al. 2014). SMARTS is a 2.5-layer reduced gravity model with 1/4° resolution that produces daily satellite-based images of ocean structure. Daily products from SMARTS have been validated against over 50 000 in situ ocean profiles between 2000 and 2010 [see Meyers et al. (2014) for full details, with further validation given in Shay et al. (2019a,b)] and the database has been widely used to study air–sea interactions and upper-ocean evolution in TCs (e.g., Jaimes et al. 2015; Jaimes de la Cruz et al. 2021; Wadler et al. 2018; Rudzin et al. 2019). The first year of the SMARTS database is 1998 and because it is satellite-based, the products do not extend all the way to the coastline. Thus, statistical relationships containing SMARTS products have smaller sample sizes than relationships that only contain TCBD observations.

In the current study, the data from SMARTS are used to represent the ocean structure prior to storm arrival. We obtain upper-ocean structure variables: mixed layer depth (MLD; defined as depth where the water is more than 0.5°C cooler than the surface), depth of the 26°C isotherm (D26), and depth of the 20°C isotherm (D20). Additionally, we obtain the ocean heat content [OHC; Eq. (3)] which is a parameter for estimating the thermal energy available in the upper ocean in TCs (also called tropical cyclone heat potential; Leipper and Volgenau 1972):

$$\mathrm{OHC} = \rho_1 c_p \int_{z=h_{26}}^{z=\eta} [T(z) - 26] dz, \tag{3}$$

where $\rho_1 = 1026$ kg m^{-3} is the reference seawater density, c_p is the specific heat at constant pressure (4.2 kJ kg^{-1} K^{-1}), $T(z)$ is the upper-ocean temperature structure that includes SST, and η is the sea surface height (in meters). Note that OHC is integrated to the 26°C isotherm here since it is the temperature typically assumed for tropical cyclogenesis (Palmén 1948) but is not a fundamental physical constraint (Cione 2015). The SMARTS data are interpolated to the location of the buoy on the date of storm passage. Sensitivity tests were conducted using ocean structure variables obtained the day before storm arrival and did not yield significantly different results because the analysis uses a window of ±5 days focusing on the specific day (not shown). Of note, while this study uses OHC since it is a readily available metric for ocean heat in the SMARTS database, Price (2009) suggested that the mean temperature in the upper 100 m ($\overline{\mathrm{T100}}$) is a more direct and robust measurement of the ocean thermal field for TCs.

In recent years, oceanic barrier layers, freshwater plumes that mostly appear in river overflow areas such as in the eastern Caribbean Sea near the Amazon–Orinoco River plume and in the Gulf of Mexico near the Mississippi River delta, have received significant attention in the air–sea interaction literature. The presence of barrier layers increases the upper-ocean stability which limits turbulent mixing of cool water into the mixed layer (e.g., Reul et al. 2014; Rudzin et al. 2017,

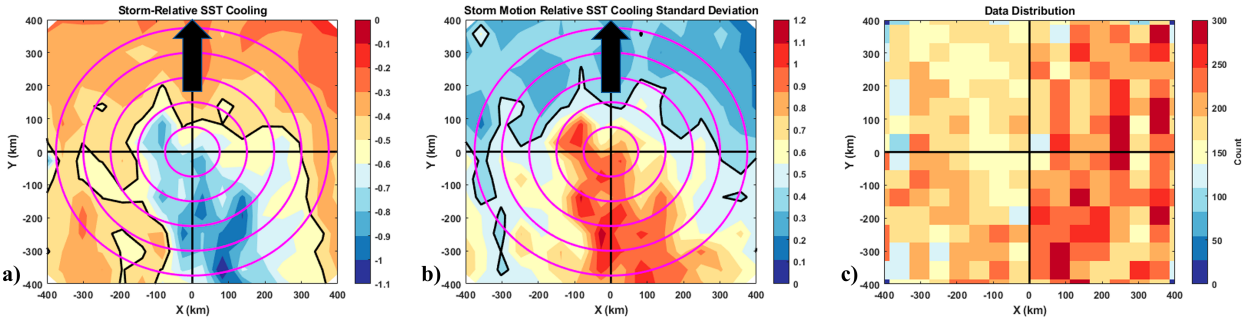

FIG. 2. (a) The spatial distributions of mean storm-relative SST cooling. (b) The standard deviation of the spatial distribution in (a). (c) The data distribution. In (a) and (b), the range rings are multiples of 75-km distance from the storm center and the arrow represents the direction of storm motion. Additionally, the 0.5°C contour is outlined in (a) and (b). Data within the innermost range ring (75 km) in (a) and (b) are used to create the predictive equations.

2018, 2019; Hlywiak and Nolan 2019; Balaguru et al. 2020; Sanabia and Jayne 2020). Since there is no long-term reliable database for upper-ocean salinity data, in this study we obtain satellite-based optimally interpolated sea surface salinity (SSS) from the Soil Moisture Active Passive (SMAP; Meissner et al. 2014) mission. Data from the SMAP mission have $^1/_4$° resolution and is produced in 4-day temporal increments. While valuable, the database only extends back to 2011, which limits the sample size for comparing with TCBD observations. We also obtain monthly climatological SSS data from the *World Ocean Atlas 2018* (*WOA18*; Zweng et al. 2018; Garcia et al. 2019). The data are also $^1/_4$° resolution averaged over the years 1981–2010, which closely coincides with what is available in the TCBD. The data are obtained in monthly climatological increments to account for seasonality of river flow. For both the *WOA18* and the SMAP mission SSS data, the global data are interpolated to the location of the buoy. Last, since SSS is only a proxy for the effect of freshwater barrier layers, which increase the stability of the layer and reduce mixing (Balaguru et al. 2020), we obtain the daily climatology of reduced gravity [Eq. (4)] from SMARTS where g^1 is reduced gravity, g is the acceleration due to gravity = 9.81 m s^{-2}, and ρ_1 and ρ_2 are the densities of the upper and lower layers, respectively, which are separated by the 20°C isotherm (Meyers et al. 2014):

$$g^1 = g \times \frac{\rho_2 - \rho_1}{\rho_2}. \tag{4}$$

3. Results

To characterize the spatial distribution of SST cooling, each SST cooling point (difference between maximum SST prior to storm arrival and SST at every observation time) is put into a storm-relative bin with a grid spacing of 55 km (Fig. 2a). Each bin has at least 50 data points, with most having at least 200 data points (Fig. 2c). As mentioned earlier, we did not place data into a normalized storm-size coordinate system (i.e., relative to the RMW) using the EBT database due to known errors with its reliability (Davis 2018). Generally, there are more data to the right of storm motion than to the left of storm motion. As expected, the maximum SST cooling occurs in the rear-right quadrant (Fig. 2a), with a maximum amplitude of 1.1°C ~400 km behind the storm track. Within the innermost 100 km of the storm center, the SST cooling typically ranges between 0.5° and 0.8°C, depending on the quadrant. In the direction of storm motion, cooling of 0.5°C typically occurs at ~100 km ahead of the storm. With the minimal amount of SST cooling ahead of the storm motion, there is also little standard deviation (Fig. 2b). The lack of cooling ahead of storm motion is consistent with Jacob et al. (2000), who showed using different ocean mixed layer models that the cooling is related to the surface friction velocity u^*. The majority of SST cooling variability occurs in the rear-right quadrant, consistent with where the maximum cooling typically occurs.

Since the goal of this manuscript is to characterize the SST cooling underneath the storm center, we define change in SST as the difference between the maximum observed initial SST (ISST) prior to storm passage (while the storm is within 555 km of the buoy) with minimum SST within 75 km of the storm center (the innermost range ring in Figs. 2a,b). The 555-km cutoff was chosen for ISST to ensure fully capturing any SST cooling due to the TC. Since the change in SST is always negative, we refer to the magnitude of the difference as SST cooling throughout the rest of the manuscript which is a positive number. Of note, the maximum SST prior to storm arrival is likely taking into account diurnal variations and may not represent a mean SST. To account for this, we repeat the analysis using a 24-h averaged SST before storm arrival (called ISST_Mean; defined as up to when the storm was within 200 km of the buoy; see section 3d). While this alternative definition of ISST may not capture all SST-induced cooling, it may be more compatible with daily-produced SST products. This is discussed further in section 3d.

The first step in creating statistical relationships for SST cooling is to characterize the distribution. Figure 3a shows the SST cooling compared to the ISST. The majority of SST cooling cases are less than 1°C and are in ISST values between 26° and 30°C. Generally, most of the distribution for SST cooling is below 4°C. However, there are SST cooling values up to 8°C, for a very high ISST value of ~32°C. A histogram of SST cooling reveals a gamma-shaped distribution that is peaked

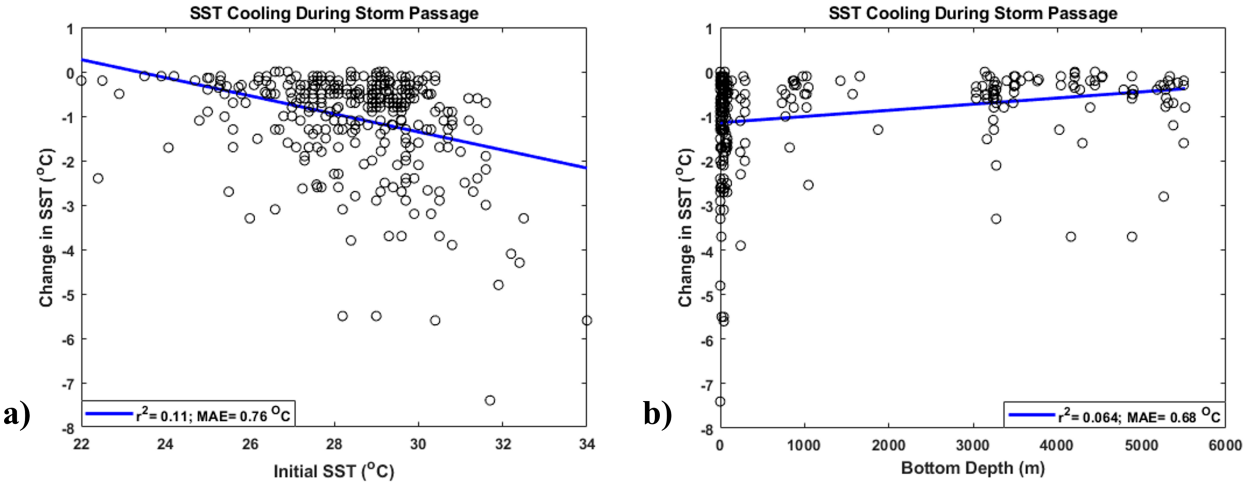

FIG. 3. A scatterplot of SST cooling within 75 km of a storm center with (a) initial SST and (b) ocean bottom depth. In each plot, the linear best fit line is given with the legend containing the coefficient of determination (r^2) and mean absolute error (MAE).

between 0° and 0.5°C of SST cooling with an extended tail out to 8°C (not shown). Further examinations of the SST cooling distribution show that there is the most spread in SST cooling in shallow water regions less than 100 m deep, which can reduce our predictive skill (Fig. 3b). Additionally, many of these higher SST cooling cases, which are in the tail of the distribution, are in shallow water. Since individual oceanic basins have unique dynamics due to bottom slope of the continental shelf and differing background currents, we eliminate all cases of bottom depth less than 100 m in the subsequent analyses in sections 3a and 3b. There are 174 remaining unique time series over deep water, of which 87 are matched with data from SMARTS and 38 are matched with data from SMAP. Separate analyses for shallow water conditions are presented in section 3c.

a. *Linear relationships between SST cooling with single variable predictors*

The relationship between SST cooling and single variable predictors in water depths greater than 100 m is given in Fig. 4. The greatest single variable predictor of SST cooling is ISST with a linear fit having an r^2 value 0.19 and a mean absolute error (MAE) of 0.7°C (Fig. 4a). Generally, there is an increased spread in SST cooling magnitudes with increased ISST. While a linear fit is able to capture the general trend of increasing average SST cooling with higher ISST values, it is unable to represent the higher SST cooling that is observed in cases with ISST greater than 30°C. Furthermore, the linear fit never predicts SST cooling greater than 2°C. While ISST values greater than 30°C are relatively rare, the large cooling magnitudes suggest that they are more often associated with shallow skin temperatures that are not representative of a mean temperature in the oceanic mixed layer. Additionally, the large spread of SST cooling at high ISST values implies cases have inhomogeneous subsurface ocean structures or different environmental setups, which motivates the use of multivariable equations to predict SST cooling. Higher-order polynomial regressions such as quadratic and cubic functions can better capture the increased SST cooling at higher ISST values and generally increase the r^2 value and decrease the MAE of the best-fit equation. However, a quadratic fit is not a reasonable regression because, as shown in Fig. 4a, it is an increasing function up to 28°C followed by a decreasing function which is not physically based. The cubic function is monotonically decreasing and can capture the observed variability at both high and low ISSTs.[1] As a single variable predictor, the third-order polynomial predicts SST cooling with an r^2 of 0.36 and a MAE of 0.58°C, which is substantially improved over the linear regression fit. Importantly, it also captures relevant physics such as the larger amounts of SST cooling that can occasionally occur at higher ISSTs (i.e., above 30°C) that represent a skin temperatures as well as the smaller amounts of SST cooling that can occasionally occur at lower ISSTs (i.e., below 26°C) which tend to occur at higher latitudes above 29°N (not shown) in more stratified (stable) ocean thermal structures. Consequences of using a cubic regression model for ISST are discussed throughout the manuscript.

The relationship between SST cooling with commonly used metrics of ocean available heat such as OHC, mixed layer depth (MLD), and depth of the 26°C isotherm (D26) are given in Figs. 4b–d. Recall that these have a smaller sample size since SMARTS analyses do not extend to the shore. A linear fit between OHC and SST cooling yields an r^2 value of 0.063 and a MAE of 0.42°C. While not offering a lot of predictive skill, OHC's relationship to SST cooling has interesting features. All of the cases of SST cooling greater than 3°C (albeit only three time series) occur in OHC values less than

[1] Of note, we tested other types of functions such as exponential fits to create the statistical relationships (not shown), but the third order polynomial consistently produced the most robust statistics and was particularly skillful at predicting SST cooling at high values of ISST.

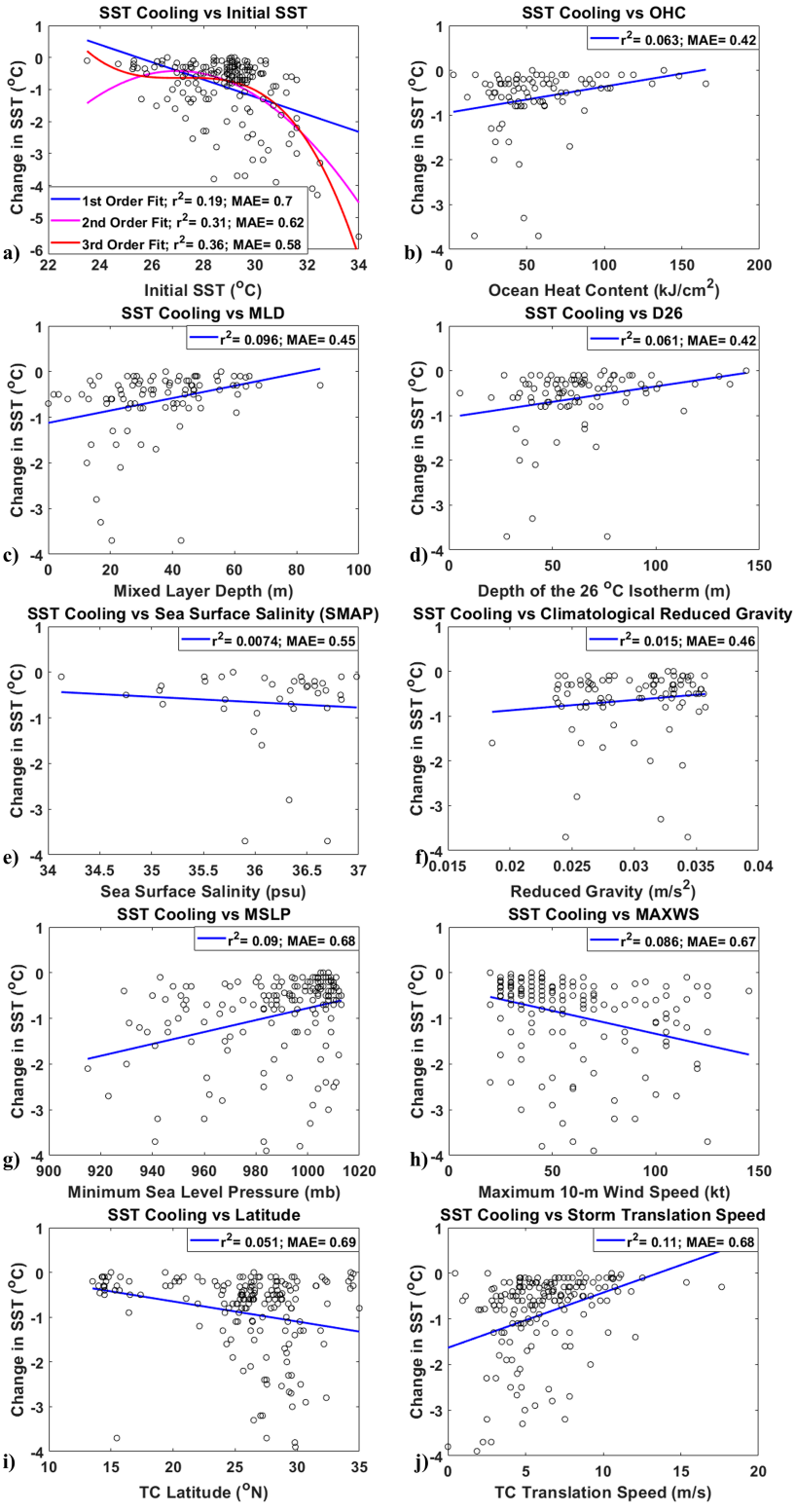

FIG. 4. Scatterplots of the relationship between SST cooling and (a) initial SST, (b) ocean heat content, (c) mixed layer depth, (d) depth of the 26°C isotherm, (e) climatological sea surface salinity from SMAP, (f) climatological reduced gravity, (g) minimum sea level pressure, (h) maximum 10-m wind speed, (i) TC latitude, and (j) TC translation speed. In each plot, the linear best fit line is given with the legend containing the coefficient of determination (r^2) and mean absolute error (MAE). In (a), the best fit quadratic and cubic functions are also shown.

60 kJ cm^{-2}. Furthermore, there is only one case of SST cooling greater than 1°C for OHC values greater than 60 kJ cm^{-2}. Combined, this yields a good "rule of thumb" that SST cooling is generally not going to exceed 1°C for OHC values greater than 60 kJ cm^{-2}. Similar, but less distinct, characteristics are noticed with MLD and D26, with the break in the distributions at 50 and 75 m, respectively.

SSS from the SMAP mission (Fig. 4e) indicates that a larger SSS (a proxy for reduced stability) is associated with more SST cooling with an r^2 value of 0.0074 and a MAE of 0.55°C. However, the sample size in Fig. 4e is limited due to the SMAP being launched in 2011. Similarly, the SSS from the WOA (not shown) shows a weak trend due to a cluster of data points between 35 and 37 psu. The daily climatology of reduced gravity from SMARTS (Fig. 4f; recall that the daily climatologies are for the average stratification at the upper thermocline which is assumed to be represented by the 20°C isotherm depth) also shows that lower reduced gravity (less stable thermocline) is associated with more cooling with an r^2 value of 0.015 and a MAE of 0.46°C. However, given the limitations of using climatological data, along with the weak statistical relationships, we do not include SSS or reduced gravity in our higher-order predictive equations. Nevertheless, the authors recommend field campaigns to obtain long-term time series of SSS so that it can be included in statistical analyses.

Since the projection of the wind stress onto the ocean surface initiates the shear-induced oceanic mixing, it is unsurprising that linear relationships indicate that lower minimum sea level pressures (MSLPs; Fig. 4g) and higher 10-m maximum wind speeds (MAXWS; Fig. 4h) leads to higher SST cooling amounts. However, as with the oceanic variables, the predictive skill is limited with r^2 values for MSLP and MAXWS of 0.09 and 0.086, respectively. Additionally, there is no dichotomy in the distributions with SST cooling amounts greater than 3°C observed at all ranges of the observed TC intensity spectrum.

SST cooling is also related to TC latitude (Fig. 4i). Even though the r^2 for the latitude distribution is 0.051, the distribution (like with OHC and MLD) provides a good rule of thumb with all but one case of SST cooling greater than 2°C occurring north of 25°N. The larger SST cooling amounts in the northern latitudes are likely because the shear-induced mixing and SST cooling are related to wind-forced near-inertial oscillations (e.g., Shay et al. 1992, 1998) whose period decreases as latitudinal distance from the equator increases (indicative of more mixing). Additionally, the upwelling response (Ekman-like dynamics) also depends on latitude, which may be a leading order during in-storm conditions, before the near-inertial cycle begins (Jaimes and Shay 2015). Last, SST cooling is related to TC translation speed (Fig. 3j). Unsurprisingly, slower-moving storms tend to have greater amounts of cooling than quicker moving storms. Translation speed provides the second highest explanation of SST cooling variance with a r^2 value of 0.11. However, cases of cooling greater than 2°C extend over a wide range of values, between 0 and 10 m s^{-1}.

b. *Relationship between SST cooling with multiple predictors*

The skill of predictive equations for SST cooling was assessed for all possible linear function combinations of two, three, four, and five variables shown in Fig. 4. Coefficients of determination for combinations of two, three, and four variables are given in Table A1 in the appendix. Combinations of four variables were subjectively determined to be best at statistically capturing the relevant physics of SST cooling without overfitting (i.e., obtaining an r^2 of approximately 1), particularly when piecewise equations are used (discussed below). An example of the statistics for four variables (ISST, OHC, MLD, and MSLP) is given in the first column of Table 1. Predicted SST cooling from the linear combination of these four variables has an r^2 of 0.44, MAE of 0.36°C, maximum predictive error of 2.4°C, and 79.3% of cases with predictive error less than 0.5°C. While a marked improvement over any of the individual variables in Fig. 4, there are still large errors up to 2.4°C, which can be problematic for statistical forecasting of TC intensity.

Recall from Fig. 4a that the maximum predicted SST cooling from a linear function over realistic ISST conditions is ~2°C. Furthermore, none of the linear relationships for predictors in Fig. 4 predicts SST cooling greater than 3°C over the range of observed predictor values. To overcome this limitation, the same four predictors in the first column of Table 1 are combined, but with a third-order fitting for ISST (second column in Table 1). Of note, when we use a third-order fitting for ISST, we obtain multiple cross-terms that capture the nonlinear relationship between the predictors. As with the single ISST predictor in Fig. 4a, changing ISST from a linear to a cubic predictor substantially improves the prediction of SST cooling with an r^2 value of 0.56, MAE of 0.29°C, maximum predictive error of 2.1°C, and 88.5% of cases with predictive error less than 0.5°C. Even with the improved values of r^2 and MAE, the largest error is still over 2°C.

To reduce the maximum errors in predicted SST cooling, which occur when there is substantial SST cooling, two separate equations were created: one for a high OHC regime ($\geq$60 kJ cm^{-2}) and one for a low OHC regime ($<$60 kJ cm^{-2}).[2] Recall from Fig. 4b that the OHC distribution bifurcates around 60 kJ cm^{-2}, which represents a rule of thumb cutoff for cases with substantial SST cooling. These piecewise functions allow for a separate SST cooling behavior for the high OHC regime, where the ocean temperature is warm to a deep enough depth such that there is only one observed case of SST cooling greater than 1°C. This also allows for a better fitting in the low OHC regime, where SST cooling greater than 2°C is observed more often. With these two equations, predictive SST cooling

[2] Note that to create piecewise functions, we tested creating piecewise functions using each variable in each equation. Using OHC to create the piecewise functions consistently led to the most robust statistics. Consistently, we tested creating piecewise functions about all OHC values that allow for significant samples using the current data sets for high OHC and low OHC regimes (cutoffs between 30 and 80 kJ cm^{-2}) and using a cutoff value of 60 kJ cm^{-2} consistently led to the most robust statistics.

TABLE 1. A comparison of statistics for different versions of the predictive equation for SST cooling containing ISST, OHC, MLD, and MSLP.

SST_cooling = f(ISST, OHC, MLD, MSLP) (N = 87)	Predictive equation with all linear terms	Predictive equation with linear terms except third-order ISST	Two predictive equations with linear terms except third-order ISST; equations are piecewise in OHC about 60 kJ cm^{-2} [predictive Eq. (1)]
Coefficient of determination (r^2)	0.44	0.56	0.80
Mean absolute error (°C)	0.36	0.29	0.23
Maximum predictive error (°C)	2.4	2.1	1.0
Percent of cases with predicted SST error < 0.5°C	79.3%	87.4%	87.4%
Equation	$\Delta SST = -0.46(ISST) + 0.013(OHC) + -0.0066(MLD) + 0.011(MSLP) + 1.7$	$\Delta SST = 6.48(MSLP) + 4.25(MLD) - 0.007(MLD \times MSLP) - 2.09(OHC) + 0.003(OHC \times MSLP) - 0.0014(OHC \times MLD) + 3.37 \times 10^{-6}(OHC \times MLD \times MSLP) + 387.02(ISST) - 0.45(ISST \times MSLP) - 0.03(ISST \times MLD) + 2.3 \times 10^{-4}(ISST \times MLD \times MSLP) + 0.042(ISST \times OHC) - 1.1 \times 10^{-4}(ISST \times OHC \times MSLP) - 7.2 \times 10^{-5}(ISST \times OHC \times MLD) - 5.59(ISST^2) + 0.0079(ISST^2 \times MSLP) - 0.0035(ISST^2 \times MLD) + 0.0013(ISST^2 \times OHC) - 0.028 \times (ISST)^3 - 5871.87$	Shown in Table A2

yields an overall r^2 value of 0.80, MAE of 0.23°C, maximum predictive error of 1.0°C, and 87.4% of cases with predictive error less than 0.5°C. While this leads to a marginal improvement in r^2 and MAE over only having a single predictive equation which is third order in ISST, the piecewise equations reduce the largest predictive error by half. Thus, the equation in the last column of Table 1 is considered the best representative of SST cooling. We identify this as predictive Eq. (1). Given the length of the predictive equations, they are provided in Table A2.

The performance of predictive Eq. (1) is given in Fig. 5a. As shown earlier, all of the situations with SST cooling greater than 2°C occur in the low OHC regime. The most noteworthy part of the performance of predictive Eq. (1) is

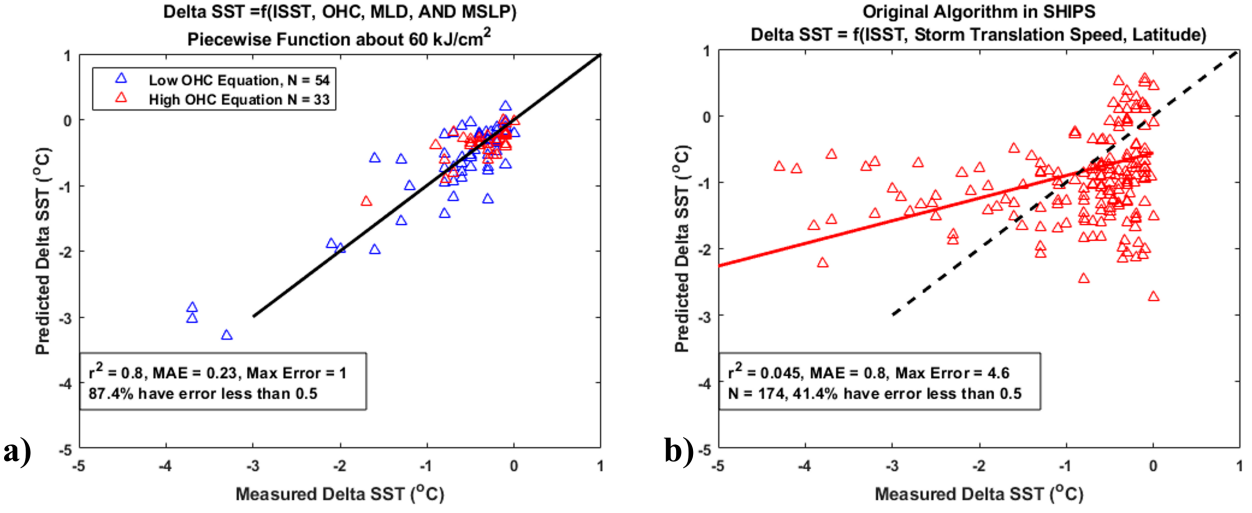

FIG. 5. (a) An evaluation of the performance of predictive Eq. (1) and (b) an evaluation of the current algorithm in SHIPS. In both panels a 1:1 line is drawn, and a best-fit line is also drawn in (b).

TABLE 2. A comparison of statistics for four different groups of variables to form a predictive equation for SST cooling. All of these equations use a cubic polynomial for the ISST distribution and a piecewise function for OHC values about 60 kJ cm^{-2}. Variables are ΔSST: change in SST, ISST: the initial prestorm SST, OHC: the ocean heat content, D26: depth of the 26°C isotherm, MSLP: minimum sea level pressure, LAT: latitude, and TSPEED: storm translation speed.

	Predictive Eq. (2): ΔSST = *f*(ISST, OHC, MSLP)	Predictive Eq. (3): ΔSST = *f*(ISST, OHC, D26, MSLP)	Predictive Eq. (4): ΔSST = *f*(ISST, OHC, MSLP, LAT)	Predictive Eq. (5): ΔSST = *f*(ISST, MSLP, TSPEED, LAT)	Predictive Eq. (6): ΔSST = *f*(ISST, OHC, TSPEED, LAT)
Coefficient of determination (r^2)	0.633	0.843	0.855	0.708	0.714
Mean absolute error (°C)	0.289	0.191	0.195	0.391	0.261
Maximum predictive error (°C)	1.85	1.304	0.887	1.763	1.274
Percent of cases with predicted SST error < 0.5°C	83.9%	95.4%	91.9%	72.9%	82.4%

that there are no extreme outliers that would impact intensity forecasts. Even so, there is reasonable spread among the data points to indicate the equations are not over fitting. To highlight the significance of the equation, the performance of the currently used SST cooling algorithm in SHIPS (linear function of ISST, translation speed, and latitude) on the current dataset is shown in Fig. 5b. Most noteworthy is that the current equation consistently underpredicts SST cooling when the actual cooling is above 1.5°C, with errors increasing as the actual SST cooling increases. As shown in Fig. 4a, this is an unavoidable occurrence with linear fitting for all variables.

With fitting ISST as a third-order function and using piecewise equations for OHC established as the best statistical methods to improve SST cooling forecasts, we evaluated all possible iterations of 2, 3, 4, and 5 variables. While predictive Eq. (1) in Table 1 is considered the best performing function, other notable ones are given in Table 2. All of the equations in Table 2 are piecewise about an OHC value of 60 kJ cm^{-2} except predictive Eq. (5), which is piecewise about a MSLP value of 985 mb (more on this below; 1 mb = 1 hPa). Note that the equations in Table 2 are not necessarily the top statistical predictions of SST cooling but allow for a diverse set of variables with the goal of testing their performance on intensity forecasts in the SHIPS model. For example, in all the equations, switching MSLP and MAXWS usually provide similar error statistics, but to avoid having equations that capture the same relevant physics, we only show equations with MSLP.

Predictive Eq. (2) (first column in Table 2; function of ISST, OHC, MSLP) is the best overall performing function that includes only three variables. While, as stated earlier, equations with four variables provide the best statistical representation of SST cooling, predictive Eq. (2) is tested to see if using four variables provides additional predictive skill for intensity forecasting. Predictive Eq. (3) generally has the lowest error statistics. With two ocean structure variables (function of ISST, OHC, D26, MSLP), it strongly encapsulates prestorm ocean structure, similar to that in predictive Eq. (1) (the only difference is MLD versus D26). Predictive Eq. (4) (function of ISST, OHC, MSLP, LATITUDE) contains the most diverse variables, capturing the storm intensity, upper-ocean thermal structure, and latitude. Predictive Eq. (5) (function of ISST, MSLP, storm translation speed, LATITUDE) is the only equation to not contain an ocean structure variable and has lower predictive ability, likely due to this fact. Since OHC is not included in this equation (which is used to separate the piecewise in all other equations), the piecewise equations are separated about a MSLP of 985 mb, which was determined to be best for these sets of variables. Predictive Eq. (6) does not have a measure of TC intensity. While this leads to lesser skill of the statistical predictive equations of SST cooling, this framework could potentially be more useful in a statistical–dynamical model such as SHIPS because of the codependent nature of SST and storm intensity (i.e., the SST cooling equations are used to predict MSLP, which is a variable in the equations themselves).

c. *Equations in shallow water regions*

As stated earlier, all of the above equations are built for areas with water depths greater than 100 m. Since these algorithms are built for use in a statistical–dynamical forecast model such as SHIPS, we still need to consider an algorithm for shallow water regions. Figure 6a shows the distribution for the SST cooling equation in shallow water with the best overall predictive skill. Since shallow water regimes cannot contain any ocean structure variables since the satellite-based products do not extend all the way to the shore, the variables used are ISST, MSLP, storm translation speed, and latitude. Like in predictive Eq. (5), ISST is fit as a third-order polynomial and there are two piecewise equations separated about a MSLP value of 985 mb. Note that the equations piecewise about 990 mb had slightly better statistics, but we show piecewise about 985 mb for equal comparison with predictive Eq. (5). The predicted SST cooling from the shallow water equation has an overall r^2 value of 0.51, MAE of 0.61°C, maximum predictive error of 3.9°C, and 51.1% of cases with predictive error less than 0.5°C.

An important question is whether there is added value to having an independent set of equations for shallow water regions. The new SST cooling equations are designed to improve intensity forecasting and storms will not spend much time over these waters before landfall which limits the effect on intensity change. More critically, imposing two different sets of equations in a model would require buffer rooms between the deep and shallow water regimes to smooth discontinuities. To assess the added value of shallow water equations,

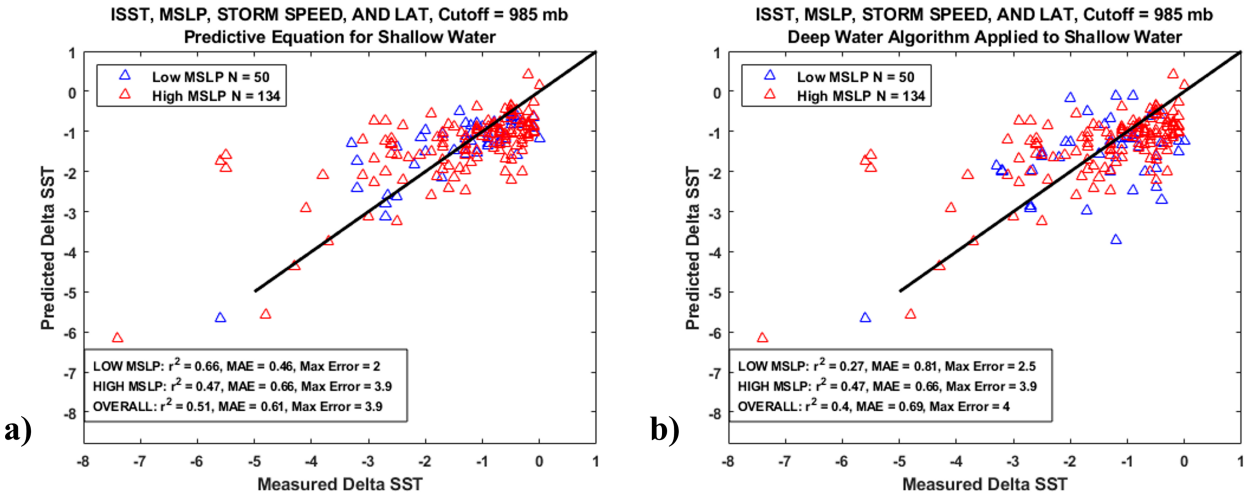

FIG. 6. A comparison between the predictive equations containing initial SST, minimum sea level pressure, storm translation speed, and latitude. (a) The equation is built using points in shallow water (ocean bottom depths less than 100 m). (b) The equation built for deep water is applied to shallow water. In both plots, the functions are piecewise for minimum sea level pressure about 985 mb, and a 1:1 line is plotted to indicate the perfect predictive equation. Statistics for each equation as well as overall statistics are displayed for each panel.

we evaluate predictive Eq. (5) for shallow water data (Fig. 6b). Using this equation, the predicted SST cooling in shallow water has an overall r^2 value of 0.40, MAE of 0.69°C, maximum predictive error of 4.0°C, and 45.7% of cases with predictive error less than 0.5°C. While there is some improvement in predictive skill, a future study should evaluate the potential benefit of having a separate equation for SST cooling for TC intensity forecasts given the aforementioned challenges of predicting SST cooling in shallow waters using statistical methods and with the relatively small degradation in MAE and maximum predictive error in SST cooling between the two equations in Fig. 6.

d. *SST cooling relationships using a 24-h mean prestorm SST*

As stated in section 3a, to be compatible with daily-produced satellite-based SST products such as the Reynolds SST (Reynolds et al. 2007), we build alternative predictive equations using a 24-h mean prestorm SST (called ISST_Mean). With SST cooling largely limited prior to 200 km ahead of storm passage (Fig. 2a), we define ISST_Mean as the 24-h averaged SST ending when the storm is within 200-km radius of a buoy. Since the predictive equations described earlier in this manuscript use an ISST that is defined as the maximum SST before storm arrival, the change in SST is always reduced when using ISST_Mean (Fig. 7a). While there is no significant trend between ISST and ISST_Mean, the latter can be up to 1.7°C cooler than ISST. The largest value of ISST_Mean is ~31°C (Fig. 7b), as opposed to 34°C for ISST, which lowers the likelihood that some of the cases represent a skin temperature and not an SST. Changing the prestorm SST definition also leads to a reduced spread in SST cooling, with more cases closer to zero, and even some cases with increasing SST during storm passage, likely due to oceanic barrier layers.

While the general trends of the correlations are similar to Fig. 4a, a consequence of the reduced spread in SST cooling is the reduced ability of the third-order polynomial to capture large changes in SST. When using ISST_Mean as a single variable predictor, the largest predicted SST cooling using a third-order polynomial is ~1.5°C, only ~0.5°C more SST cooling than using a linear relationship. Similar trends for SST cooling appear for all single variable predictors using ISST_Mean as in Fig. 4 (not shown), though there are mixed statistical differences with both a lower r^2 value and a lower MAE with using ISST_Mean.

The lack of an ability to capture the high SST cooling cases when using a higher-order polynomial for ISST_Mean leads to an underprediction of SST cooling in the final predictive equations that use four variables when the actual cooling is high (Fig. 7c). Overall, when using the same variables as predictive Eq. (1) (and Fig. 5a), the r^2 is lower and maximum error is higher (1.4° vs 1.0°C) when using ISST_Mean. Additionally, the underprediction of large SST cooling cases does not fix the same issue using the current algorithm utilized in SHIPS (Fig. 5b). However, the lower spread in SST cooling when using ISST_Mean leads to a greater percent of cases have a forecasted SST error less than 0.5°C (93.1% vs 87.4%). Since an end user of the predictive equations may want to compare the tradeoffs of more cases of increased accuracy, but larger potential errors and an underprediction of large SST cooling cases when using ISST_Mean (as opposed to ISST) for a prestorm SST, we provide predictive equations using the same set as variables as using ISST in Table A3.

4. Discussion and conclusions

Since the early theories for TC intensification (e.g., Malkus and Riehl 1960; Emanuel 1986), the SST has been identified as a key metric for TCs because it relates to the surface

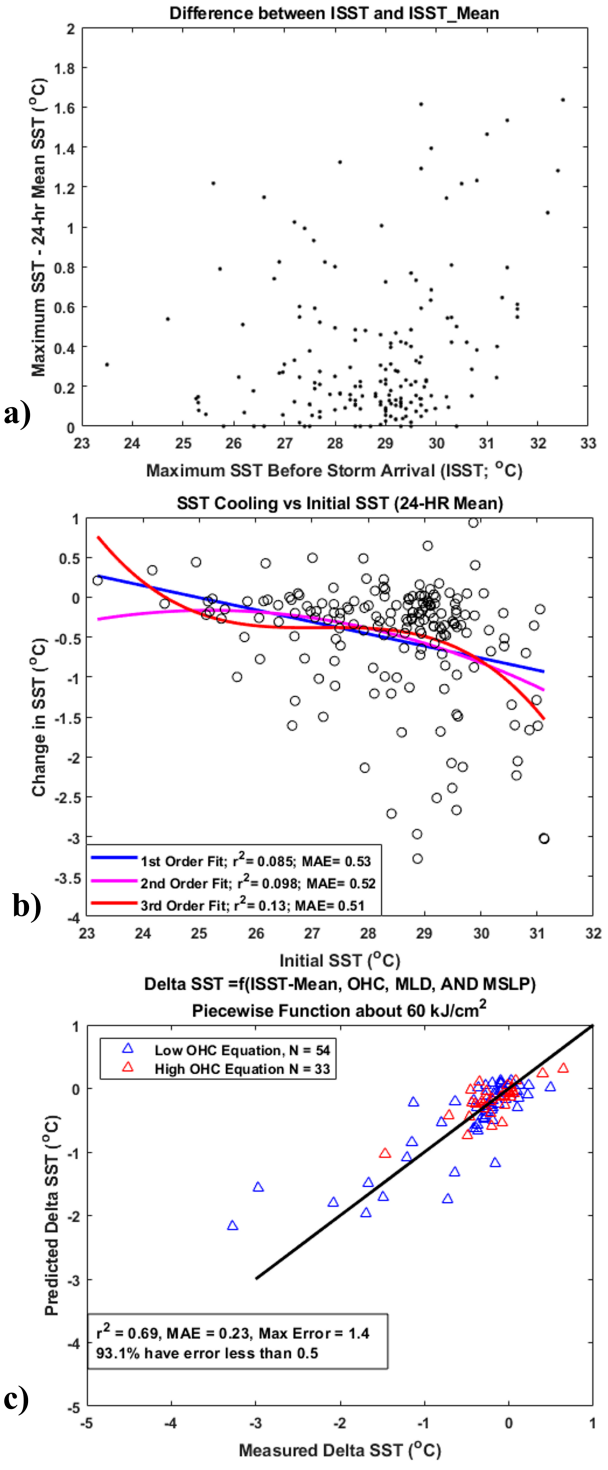

FIG. 7. (a) The comparison of maximum prestorm SST (ISST) with the difference between the 24-h mean SST prior to storm arrival (ISST_Mean). (b) As in Fig. 4a, but using ISST_Mean as a prestorm SST. (c) As in Fig. 5a, but for using ISST_Mean as a prestorm SST.

sensible heat and latent heat fluxes. However, to date, no reliable instrument platform has been established to continuously measure the SST in the inner core of a TC as it translates across ocean basins. Satellite-based SST products provide the greatest spatial distribution of measurements. However, satellite-based measurements are notoriously unreliable in cloudy conditions, which means the SST cooling cannot be accurately measured at a given location during storm passage. Aircraft-based expendables (e.g., AXBTs, drifters) can measure the in-storm SST, but their use is limited to TCs sampled by reconnaissance aircraft and provide no information on the quiescient, initial SST conditions prior to storm passage. Long duration motorized autonomous vehicles (saildrones, gliders) and Lagrangian floats can sample the evolution of the upper ocean, but generally traverse too slowly to stay in the inner core of a TC. With the limitations of these observational platforms, prediction of inner-core SST using statistical methods becomes highly desirable.

While there is a lot of literature about the cold wake SST, or SST cooling that occurs multiple inertial periods after storm passage, significantly less research exists related to SST cooling directly under the storm core. In-storm SST cooling was documented by Cione and Uhlhorn (2003) using buoy time series for 23 Atlantic, Gulf of Mexico, and Caribbean TCs between 1975 and 2002. Based on the results from Cione and Uhlhorn (2003), an SST cooling algorithm was created for the SHIPS operational forecast model. With the buoy database expanded to include time series through 2017, this study evaluated and updated the SST cooling algorithms such that they can potentially be used in existing statistical–dynamical models (e.g., SHIPS, LGEM, RI index).

The first step to building an SST cooling algorithm is to evaluate how individual predictors relate to SST cooling. All the predictors were evaluated for water depths greater than 100 m to eliminate coastal dynamics of each basin which cannot be accounted for in statistical modeling. The best predictor for SST cooling using a linear function is the maximum prestorm SST (ISST). However, using a linear regression model does not encapsulate the enhanced SST cooling at higher (~greater than 30°C) ISST values, and a third-order regression model was deemed to best model the observed ocean behavior. The predicted SST cooling from the OHC, derived from the SMARTS database (Meyers et al. 2014), has a lower r^2 value than the ISST. However, OHC provides a good "rule of thumb" with only one case of SST cooling greater than 1°C occurring in OHC values greater than 60 kJ cm^{-2}. There are similar conclusions about other ocean structure variables: MLD, D26, and D20.

Another variable that has received a lot attention in the literature is sea surface salinity (SSS) because freshwater can increase stability, which reduces turbulent mixing of cooler waters into the oceanic mixed layer. Without a long-term database, we tested the relationship between SST cooling with: SSS values measured from the SMAP mission that only goes back to 2011, monthly climatological SSS values from the WOA, and a daily climatology of reduced gravity from SMARTS which can capture changes to the upper-ocean stratification due to freshwater. With these limited databases,

no salinity or ocean stratification product had a strong relationship to SST cooling. Thus, it was not able to be included in the statistical relationships.

The last variables tested were storm parameters such as MSLP, MAXWS, latitude, and storm translation speed. The strongest linear relationship between SST cooling and these variables is storm translation speed, with an r^2 value of 0.11 and a MAE of 0.68°C. While the linear relationship is not as strong, all the SST cooling values except one greater than 2°C occur in latitudes higher than 25°N. SST cooling values greater than 2°C occur over large ranges of MSLP and MAXWS values, signifying that storm intensity alone is a weak predictor for SST cooling.

Predictive equations were built using two, three, four, and five of the variables described above. We determined that the combination of four variables generally led to the best prediction of SST cooling without overfitting (i.e., obtaining a r^2 of approximately 1). For all the predictive equations, fitting ISST as a third-order function and having piecewise functions for OHC regimes higher and lower than 60 kJ cm^{-2} led to the best statistical relationships. The top predictive equations take into account the ISST, information about the upper-ocean thermal structure (e.g., OHC, MLD, D26), the storm intensity, and latitude. Of note, using either MSLP or MAXWS for storm intensity in predictive equation yields very similar predictive skill. These variables are consistent with what was deemed important for in-storm SST cooling using linear theory in Lu et al. (2021). In total, six predictive equations were deemed to best predict SST cooling, with the overall most representative being a function of ISST, OHC, MLD, and MSLP. As compared to the current SST cooling equation in SHIPS, the new equation eliminates a low bias in SST cooling when the actual SST cooling is large. The low bias primarily in the current equation is due to the equation being linear. Of note, we repeated the above analysis, using a 24-h averaged prestorm SST (ISST_Mean). Using ISST_Mean, there was a reduced range of SST cooling outcomes and the higher-order polynomial was unable to capture large changes in SST. Thus, predictive equations using ISST_Mean had more cases with error less than 0.5°C, but had larger maximum errors and an underprediction of SST cooling when the actual cooling was large. Last, we derived a separate equation for shallow water (<100-m depth), but the improvements over the deep-water equations were not significant which is likely due to the complex bathymetry and dynamics unique to each shallow-water region.

We suggest a follow up study to evaluate the performance of these equations for TC intensity forecasts in a statistical–dynamical model such as SHIPS (and perhaps other models including LGEM and the RI index). Preliminary evaluations with the SHIPS science team indicate that one must be careful about applying nonlinear equations outside of the domain they were built in. It is important to note that these equations are neither meant to perfectly forecast the SST cooling at any given location nor account for all possible physical factors potentially in play. For example, this analysis did not include the effects of radiation on the SST cooling. Regardless of the implication of the equations, the results in this manuscript demonstrate how SST cooling underneath a storm is related to the initial SST, the ocean structure, the latitude (inertial period), and the strength and translation speed of the storm. Last, due to sample size constraints, we only created predictive equations for underneath the inner core of a TC, but future work with larger datasets can create predictive relationships for SST at different radii and azimuths.

Acknowledgments. The authors greatly appreciate the comments and insights from Mark DeMaria, Galina Chirokova, and John Kaplan for discussions about SHIPS model and how to implement SST cooling equations into that infrastructure. J. Wadler was generously supported by the ERAU Faculty Innovative Research in Science and Technology (FIRST) Program and the NOAA Office of Marine and Aviation Operations Uncrewed Systems Office. S. Michlowitz was supported on this project by the NOAA Hollings Program. We greatly appreciate NOAA's NDBC for the hard task of maintaining the buoys at sea. The comments from three anonymous reviewers greatly helped to improve the manuscript.

Data availability statement. NDBC data are freely available at https://www.ndbc.noaa.gov/ and SHIPS data are available at https://rammb2.cira.colostate.edu/research/tropical-cyclones/ships. Parties interested in obtaining other observations associated with the TCBD should contact Joseph Cione (joe.cione@noaa.gov).

APPENDIX

Predictive SST Cooling Equations

Table A1 shows the coefficient of determination for all linear best-fit lines for all combinations of 2, 3, and 4 variables. Tables A2 and A3 show the final predictive equations using ISST and ISST_Mean, respectively. Both Tables A2 and A3 also show the final predictive equation for shallow water for their respective prestorm SST definition.

TABLE A1. A comparison of coefficient of determination (r^2) values for all combinations of 2, 3, and 4 variable predictors.

Two variable predictors			Three variable predictors				Four variable predictors				
Var 1	Var 2	r^2	Var 1	Var 2	Var 3	r^2	Var 1	Var 2	Var 3	Var 4	r^2
ISST	OHC	0.287	ISST	OHC	MLD	0.304	ISST	OHC	MLD	D26	0.345
ISST	MLD	0.134	ISST	OHC	D26	0.345	ISST	OHC	MLD	MSLP	0.442
ISST	D26	0.175	ISST	OHC	MSLP	0.435	ISST	OHC	MLD	MAX wind speed	0.435
ISST	MSLP	0.262	ISST	OHC	MAX wind speed	0.425	ISST	OHC	MLD	Storm speed	0.332
ISST	MAX wind speed	0.251	ISST	OHC	Storm speed	0.318	ISST	OHC	MLD	TC LAT	0.306
ISST	Storm speed	0.239	ISST	OHC	TC LAT	0.287	ISST	OHC	D26	MSLP	0.478
ISST	TC LAT	0.269	ISST	MLD	D26	0.175	ISST	OHC	D26	MAX wind speed	0.468
OHC	MLD	0.098	ISST	MLD	MSLP	0.311	ISST	OHC	D26	Storm speed	0.376
OHC	D26	0.07	ISST	MLD	MAX wind speed	0.289	ISST	OHC	D26	TC LAT	0.348
OHC	MSLP	0.218	ISST	MLD	Storm speed	0.187	ISST	OHC	MSLP	MAX wind speed	0.435
OHC	MAX wind speed	0.203	ISST	MLD	TC LAT	0.147	ISST	OHC	MSLP	Storm speed	0.464
OHC	Storm speed	0.179	ISST	D26	MSLP	0.348	ISST	OHC	MSLP	TC LAT	0.435
OHC	TC LAT	0.088	ISST	D26	MAX wind speed	0.333	ISST	OHC	MAX wind speed	Storm speed	0.457
MLD	D26	0.085	ISST	D26	Storm speed	0.218	ISST	OHC	MAX wind speed	TC LAT	0.425
MLD	MSLP	0.272	ISST	D26	TC LAT	0.176	ISST	OHC	Storm speed	TC LAT	0.318
MLD	MAX wind speed	0.252	ISST	MSLP	MAX wind speed	0.265	ISST	MLD	D26	MSLP	0.35
MLD	Storm speed	0.174	ISST	MSLP	Storm speed	0.331	ISST	MLD	D26	MAX wind speed	0.334
MLD	TC LAT	0.113	ISST	MSLP	TC LAT	0.352	ISST	MLD	D26	Storm speed	0.219
D26	MSLP	0.228	ISST	MAX wind speed	Storm speed	0.318	ISST	MLD	D26	TC LAT	0.176
D26	MAX wind speed	0.213	ISST	MAX wind speed	TC LAT	0.339	ISST	MLD	MSLP	MAX wind speed	0.313
D26	Storm speed	0.159	ISST	Storm speed	TC LAT	0.294	ISST	MLD	MSLP	Storm speed	0.358
D26	TC LAT	0.075	OHC	MLD	D26	0.101	ISST	MLD	MSLP	TC LAT	0.318
MSLP	MAX wind speed	0.09	OHC	MLD	MSLP	0.266	ISST	MLD	MAX wind speed	Storm speed	0.34
MSLP	Storm speed	0.221	OHC	MLD	MAX wind speed	0.248	ISST	MLD	MAX wind speed	TC LAT	0.297
MSLP	TC LAT	0.152	OHC	MLD	Storm speed	0.193	ISST	MLD	Storm speed	TC LAT	0.192
MAX wind speed	Storm speed	0.215	OHC	MLD	TC LAT	0.105	ISST	D26	MSLP	MAX wind speed	0.348
MAX wind speed	TC LAT	0.144	OHC	D26	MSLP	0.229	ISST	D26	MSLP	Storm speed	0.388
Storm speed	TC LAT	0.135	OHC	D26	MAX wind speed	0.215	ISST	D26	MSLP	TC LAT	0.348
			OHC	D26	Storm speed	0.179	ISST	D26	MAX wind speed	Storm speed	0.376
			OHC	D26	TC LAT	0.088	ISST	D26	MAX wind speed	TC LAT	0.333
			OHC	MSLP	MAX wind speed	0.218	ISST	D26	Storm speed	TC LAT	0.218
			OHC	MSLP	Storm speed	0.332	ISST	MSLP	MAX wind speed	Storm speed	0.332
			OHC	MSLP	TC LAT	0.239	ISST	MSLP	MAX wind speed	TC LAT	0.353
			OHC	MAX wind speed	Storm speed	0.322	ISST	MSLP	Storm speed	TC LAT	0.388
			OHC	MAX wind speed	TC LAT	0.225	ISST	MAX wind speed	Storm speed	TC LAT	0.378
			OHC	Storm speed	TC LAT	0.184	OHC	MLD	D26	MSLP	0.269
			MLD	D26	MSLP	0.263	OHC	MLD	D26	MAX wind speed	0.25
			MLD	D26	MAX wind speed	0.244	OHC	MLD	D26	Storm speed	0.204
			MLD	D26	Storm speed	0.175	OHC	MLD	D26	TC LAT	0.11
			MLD	D26	TC LAT	0.091	OHC	MLD	MSLP	MAX wind speed	0.266
			MLD	MSLP	MAX wind speed	0.273	OHC	MLD	MSLP	Storm speed	0.355

TABLE A1. (*Continued*)

Two variable predictors			Three variable predictors				Four variable predictors				
Var 1	Var 2	r^2	Var 1	Var 2	Var 3	r^2	Var 1	Var 2	Var 3	Var 4	r^2
			MLD	MSLP	Storm speed	0.344	OHC	MLD	MSLP	TC LAT	0.269
			MLD	MSLP	TC LAT	0.282	OHC	MLD	MAX wind speed	Storm speed	0.344
			MLD	MAX wind speed	Storm speed	0.327	OHC	MLD	MAX wind speed	TC LAT	0.252
			MLD	MAX wind speed	TC LAT	0.263	OHC	MLD	Storm speed	TC LAT	0.194
			MLD	Storm speed	TC LAT	0.18	OHC	D26	MSLP	MAX wind speed	0.23
			D26	MSLP	MAX wind speed	0.228	OHC	D26	MSLP	Storm speed	0.332
			D26	MSLP	Storm speed	0.324	OHC	D26	MSLP	TC LAT	0.242
			D26	MSLP	TC LAT	0.238	OHC	D26	MAX wind speed	Storm speed	0.323
			D26	MAX wind speed	Storm speed	0.313	OHC	D26	MAX wind speed	TC LAT	0.228
			D26	MAX wind speed	TC LAT	0.224	OHC	D26	Storm speed	TC LAT	0.185
			D26	Storm speed	TC LAT	0.162	OHC	MSLP	MAX wind speed	Storm speed	0.332
			MSLP	MAX wind speed	Storm speed	0.221	OHC	MSLP	MAX wind speed	TC LAT	0.239
			MSLP	MAX wind speed	TC LAT	0.152	OHC	MSLP	Storm speed	TC LAT	0.336
			MSLP	Storm speed	TC LAT	0.251	OHC	MAX wind speed	Storm speed	TC LAT	0.327
			MAX wind speed	Storm speed	TC LAT	0.247	MLD	D26	MSLP	MAX wind speed	0.263
							MLD	D26	MSLP	Storm speed	0.349
							MLD	D26	MSLP	TC LAT	0.265
							MLD	D26	MAX wind speed	Storm speed	0.335
							MLD	D26	MAX wind speed	TC LAT	0.247
							MLD	D26	Storm speed	TC LAT	0.176
							MLD	MSLP	MAX wind speed	Storm speed	0.344
							MLD	MSLP	MAX wind speed	TC LAT	0.283
							MLD	MSLP	Storm speed	TC LAT	0.346
							MLD	MAX wind speed	Storm speed	TC LAT	0.331
							D26	MSLP	MAX wind speed	Storm speed	0.324
							D26	MSLP	MAX wind speed	TC LAT	0.239
							D26	MSLP	Storm speed	TC LAT	0.325
							D26	MAX wind speed	Storm speed	TC LAT	0.315
							MSLP	MAX wind speed	Storm speed	TC LAT	0.251

TABLE A2. A table of the SST predictive equations created in the manuscript. Of note, the equations are written in MATLAB syntax, so a dot in front of an operator indicates an element-wise operation.

Predictive Eq. (1)	IF OHC<=60
Delta_SST = *f*(x1 = ISST, x2 = OHC, x3 = MLD, x4 = MSLP)	@(x1,x2,x3,x4) + 6.9436619.*x4+−33.427523.*x3 + 0.01387629.*x3.*x4 + 63.244107.*x2+−0.057074202.*x2.*x4+−0.056831412.*x2.*x3 + 9.1903726e-05.*x2.*x3.*x4 + 306.33804.*x1+−0.4250965.*x1.*x4 + 1.998559.*x1.* x3+−0.00062327816.*x1.*x3.*x4+−2.4100781.*x1.*x2 + 0.0018982352.*x1.*x2.*x4+−0.0012152313.*x1.*x2.*x3+−2.1550766.*x1.^2 + 0.0065130921.*x1.^2.*x4+−0.024201002.*x1.^2.*x3 + 0.010371682.*x1.^2.*x2+−5849.4223.*1+−0.054014451.*x1.^3
	IF OHC>60
	@(x1,x2,x3,x4) + 34.5719996.*x4 + 21.2029048.*x3+−0.0196512659.*x3.*x4+−22.9444119.*x2 + 0.0207946141.*x2.*x4+−0.00768116675.*x2.*x3 + 2.37796235e-06.*x2.*x3.*x4 + 2100.41087.*x1+−2.41682892.*x1.*x4+−0.786422129.*x1.*x3 + 0.000674778977.*x1.*x3.*x4 + 0.871443085.*x1.*x2+−0.000714016613.*x1.*x2.*x4 + 0.000183697645.*x1.*x2.*x3+−31.8100404.*x1.^2 + 0.0422141446.*x1.^2.*x4 + 0.00199140006.*x1.^2.*x3+−0.00286693526.*x1.^2.*x2+−31366.2389.*1+−0.113974699.*x1.^3
Predictive Eq. (2)	IF OHC<=60
Delta_SST = *f*(x1 = ISST, x2 = OHC, x3 = MSLP)	@(x1,x2,x3) + −1.3926958.*x3 + 14.367177.*x2+−0.012636651.*x2.*x3+−103.90755.*x1 + 0.1106579.*x1.*x3+−0.60033536.*x1.*x2 + 0.00046094506.*x1.*x2.*x3 + 2.1733786.*x1.^2+−0.002177312.*x1.^2.*x3 + 0.0027820378.*x1.^2.*x2 + 1274.534.*1+−0.0031188281.*x1.^3
	IF OHC>60
	@(x1,x2,x3) + 24.0380889.*x3+−22.3879585.*x2 + 0.0172793372.*x2.*x3 + 1405.60748.*x1+−1.71011642.*x1.*x3 + 0.932499136.*x1.*x2+−0.00058764566.*x1.*x2.*x3+−20.4524081.*x1.^2 + 0.0303615465.*x1.^2.*x3+−0.00581328192.*x1.^2.*x2+−20921.9752.*1+−0.107407925.*x1.^3
Predictive Eq. (3)	IF OHC<=60
Delta_SST = *f*(x1 = ISST, x2 = OHC, x3 = D26, x4 = MSLP)	@(x1,x2,x3,x4) + 10.6485202.*x4 + 8.57762034.*x3 + 0.0125136031.*x3.*x4 + 1.1862148.*x2+−0.0143065006.*x2.*x4+−0.051586209.*x2.*x3 + 9.09499371e-05.*x2.*x3.*x4 + 1004.07383.*x1+−0.755861502.*x1.*x4+−0.950342567.*x1.*x3+−0.000562883674.*x1.*x3.*x4 + 0.512115344.*x1.*x2 + 0.000330511211.*x1.*x2.*x4+−0.00137418272.*x1.*x2.*x3+−21.4034106.*x1.^2 + 0.0136379476.*x1.^2.*x4 + 0.0271052768.*x1.^2.*x3+−0.0133962962.*x1.^2.*x2+−13241.3553.*1 + 0.0788739494.*x1.^3
	IF OHC>60
	@(x1,x2,x3,x4) + 35.4814552.*x4 + 8.26625742.*x3+−0.0599710779.*x3.*x4+−38.1797615.*x2 + 0.0719389865.*x2.*x4+−0.0152872693.*x2.*x3 + 5.80301834e-06.*x2.*x3.*x4 + 462.031233.*x1+−2.48564738.*x1.*x4 + 1.52942015.*x1.*x3 + 0.00204157934.*x1.*x3.*x4 + 0.194278396.*x1.*x2+−0.0024862272.*x1.*x2.*x4 + 0.000325351936.*x1.*x2.*x3 + 24.6815421.*x1.^2 + 0.0435663634.*x1.^2.*x4+−0.0616712684.*x1.^2.*x3 + 0.0389111247.*x1.^2.*x2+−15500.4356.*1+−0.766453038.*x1.^3
Predictive Eq. (4)	IF OHC<=60
Delta_SST = *f*(x1 = ISST, x2 = OHC, x3 = MSLP, x4 = LATITUDE)	@(x1,x2,x3,x4) + −126.4253.*x4 + 5.182775.*x3 + 0.0330316.*x3.*x4+−1.34145.*x2+−0.008530941.*x2.*x4 + 0.01503597.*x2.*x3+−0.0001739394.*x2.*x3.*x4 + 27.6741.*x1 + 7.958869.*x1.*x4+−0.4190176.*x1.*x3+−0.001001465.*x1.*x3.*x4+−0.4504566.*x1.*x2 + 0.006595046.*x1.*x2.*x4+−0.000370415.*x1.*x2.*x3 + 2.923315.*x1.^2+−0.1294736.*x1.^2.*x4 + 0.008188432.*x1.^2.*x3 + 0.01177633.*x1.^2.*x2+−847.0457.*1+−0.09510695.*x1.^3
	IF OHC>60
	@(x1,x2,x3,x4) + 140.264671.*x4 + 15.4237518.*x3+−0.155903464.*x3.*x4 + 30.465315.*x2 + 0.0563635586.*x2.*x4+−0.0127297001.*x2.*x3 + 1.59013936e-05.*x2.*x3.*x4 + 787.732311.*x1+−4.35794232.*x1.*x4+−0.893204609.*x1.*x3 + 0.00533639419.*x1.*x3.*x4+−1.68015028.*x1.*x2+−0.00246502568.*x1.*x2.*x4 + 0.000429819533.*x1.*x2.*x3+−7.97577815.*x1.^2+−0.0152162285.*x1.^2.*x4 + 0.0124853872.*x1.^2.*x3 + 0.0220157793.*x1.^2.*x2+−14646.9689.*1+−0.0619282982.*x1.^3
Predictive Eq. (5)	IF MSLP<=985
Delta_SST = *f*(x1 = ISST, x2 = MSLP, x3 = STORM SPEED, x4 = LATITUDE)	@(×1,x2,x3,x4) + −135.88253.*x4+−30.312011.*x3+−1.195269.*x3.*x4+−5.6791571.*x2 + 0.15430333.*x2.*x4 + 0.010123488.*x2.*x3 + 0.00068381148.*x2.*x3.*x4+−275.09857.*x1 + 4.6325659.*x1.*x4 + 2.7074664.*x1.*x3 + 0.017524558.*x1.*x3.*x4 + 0.23588608.*x1.*x2+−0.0055744728.*x1.*x2.*x4+−0.0007500941.*x1.*x2.*x3 + 3.1186802.*x1.^2 + 0.010344265.*x1.^2.*x4+−0.04280651.*x1.^2.*x3+−0.0011861908.*x1.^2.*x2 + 5801.2451.*1+−0.024958009.*x1.^3
	IF MSLP>985
	@(x1,x2,x3,x4) + −40.864903.*x4+−21.267591.*x3 + 1.3675633.*x3.*x4+−0.59145086.*x2 + 0.038790321.*x2.*x4 + 0.024442491.*x2.*x3+−0.0016657316.*x2.*x3.*x4+−108.16384.*x1 + 1.2181939.*x1.*x4+−0.21324181.*x1.*x3 + 0.010970859.*x1.*x3.*x4+−0.0029472393.*x1.*x2+−0.00099130535.*x1.*x2.*x4 + 0.00024033753.*x1.*x2.*x3 + 3.2664319.*x1.^2+−0.0055661847.*x1.^2.*x4+−0.0051903209.*x1.^2.*x3 + 0.0005944699.*x1.^2.*x2 + 1636.4917.*1+−0.0437288.*x1.^3

TABLE A2. (*Continued*)

Predictive Eq. (6)	IF OHC<=60
Delta_SST = *f*(x1 = ISST, x2 = OHC, x3 = STORM SPEED (m s^{-1}), x4 = LATITUDE)	@(x1,x2,x3,x4) + 30.84379.*x4 + 132.96518.*x3 + 0.2373509.*x3.*x4 + 25.883353.*x2+−0.084529611.*x2.*x4+−0.22099567.*x2.*x3+−0.0011999698.*x2.*x3.*x4 + 199.09073.*x1+−2.1333468.*x1.*x4+−9.3645509.*x1.*x3+−0.006570972.*x1.*x3.*x4+−1.717113.*x1.*x2 + 0.0034007053.*x1.*x2.*x4 + 0.0089100852.*x1.*x2.*x3+−3.6878833.*x1.^2 + 0.036163757.*x1.^2.*x4 + 0.16307656.*x1.^2.*x3 + 0.027980046.*x1.^2.*x2+−2790.5599.*1 + 0.0054993075.*x1.^3
	IF OHC>60
	@(x1,x2,x3,x4) + −29.3749631.*x4 + 74.3495696.*x3+−0.404942718.*x3.*x4 + 13.9333152.*x2 + 0.11908507.*x2.*x4 + 0.0733093834.*x2.*x3+−2.72754406e-05.*x2.*x3.*x4 + 1035.43002.*x1 + 1.86741299.*x1.*x4+−4.89842088.*x1.*x3 + 0.0141589264.*x1.*x3.*x4+−1.05240501.*x1.*x2+−0.00403138961.*x1.*x2.*x4+−0.00242602385.*x1.*x2.*x3+−34.5751003.*x1.^2+−0.0296904893.*x1.^2.*x4 + 0.0800944356.*x1.^2.*x3 + 0.0196564195.*x1.^2.*x2+−10294.1716.*1 + 0.383330478.*x1.^3
Shallow water predictive equation	IF MSLP<=985
Delta_SST = *f*(x1 = ISST, x2 = MSLP, x3 = STORM SPEED, x4 = LATITUDE)	@(x1,x2,x3,x4) + −26.724287.*x4 + 66.916018.*x3+−1.9076994.*x3.*x4+−4.8440546.*x2 + 0.0081996127.*x2.*x4+−0.031723382.*x2.*x3 + 0.0012554869.*x2.*x3.*x4+−343.47352.*x1 + 1.9717191.*x1.*x4+−1.4843114.*x1.*x3 + 0.024518816.*x1.*x3.*x4 + 0.32618279.*x1.*x2+−0.00048211325.*x1.*x2.*x4+−0.0003654624.*x1.*x2.*x3 + 5.5658943.*x1.^2+−0.029771321.*x1.^2.*x4 + 0.019828937.*x1.^2.*x3+−0.0052260253.*x1.^2.*x2 + 5030.1538.*1 + 0.0016209537.*x1.^3
	IF MSLP>985
	@(x1,x2,x3,x4) + −286.82335.*x4+−36.4868214.*x3+−0.303936264.*x3.*x4+−13.2189813.*x2 + 0.305495913.*x2.*x4 + 0.0627888391.*x2.*x3+−0.000310948656.*x2.*x3.*x4+−563.810952.*x1 + 9.4542871.*x1.*x4 + 0.899621075.*x1.*x3 + 0.0228238679.*x1.*x3.*x4 + 0.576695403.*x1.*x2+−0.0106227791.*x1.*x2.*x4+−0.00218173773.*x1.*x2.*x3 + 4.34662958.*x1.^2 + 0.0176153579.*x1.^2.*x4 + 0.0114815898.*x1.^2.*x3+−0.00396021805.*x1.^2.*x2 + 12835.3474.*1+−0.0125266855.*x1.^3

TABLE A3. As in Table A2, but using a 24-h mean prestorm SST (ISST_Mean) instead of the maximum prestorm SST (ISST). Of note, the equations are written in MATLAB syntax, so a dot in front of an operator indicates an element-wise operation.

Predictive Eq. (1) Delta_SST = *f*(x1 = ISST_Mean, x2 = OHC, x3 = MLD, x4 = MSLP)	IF OHC<=60 @(x1,x2,x3,x4) + -1.9160562.*x4+−29.056139.*x3 + 0.024400487.*x3.*x4 + 25.895754.*x2+ −0.022892469.*x2.*x4+−0.093659847.*x2.*x3 + 9.5455209e-05.*x2.*x3.*x4+−265.34708.*x1 + 0.13636362.*x1.*x4 + 1.3311489.*x1.*x3+−0.00098868553.*x1.*x3.*x4+−0.93766597.*x1.*x2 + 0.00070771313.*x1.*x2.*x4+−7.3643093e-05.*x1.*x2.*x3 + 7.0205213.*x1.^2+−0.0022867748.*x1.^2.* x4+−0.006292974.*x1.^2.*x3 + 0.0044163735.*x1.^2.*x2 + 3091.5508.*1+−0.058130676.*x1.^3 IF OHC>60 @(x1,x2,x3,x4) + 44.9417786.*x4 + 57.8217806.*x3+−0.0375417357.*x3.*x4+−38.7620801.*x2 + 0.0246436615.*x2.*x4+−0.0169120038.*x2.*x3 + 2.81370896e-05.*x2.*x3.*x4 + 3685.78638.*x1+ −3.13722219.*x1.*x4+−2.63903664.*x1.*x3 + 0.00122323197.*x1.*x3.*x4 + 1.82356742.*x1.*x2+ -0.000896685732.*x1.*x2.*x4+−0.000364670757.*x1.*x2.*x3+−73.4713927.*x1.^2 + 0.0548625314.* x1.^2.*x4 + 0.0246333731.*x1.^2.*x3+−0.0152179674.*x1.^2.*x2+−50299.0621.*1 + 0.209204646.*x1.^3
Predictive Eq. (2) Delta_SST = *f*(x1 = ISST_Mean, x2 = OHC, x3 = MSLP)	IF OHC<=60 @(x1,x2,x3) + -6.4643864.*x3+−14.334783.*x2 + 0.012350524.*x2.*x3+−513.70413.*x1 + 0.43715062.*x1.*x3 + 0.53991079.*x1.*x2+−0.00040625044.*x1.*x2.*x3 + 10.041042.*x1.^2+ −0.0073915355.*x1.^2.*x3+−0.0022242977.*x1.^2.*x2 + 7205.3391.*1+−0.030768788.*x1.^3 IF OHC>60 @(x1,x2,x3) + 24.0806952.*x3+−27.691898.*x2 + 0.0237817587.*x2.*x3 + 1509.7407.*x1+ −1.74805685.*x1.*x3 + 1.07785472.*x1.*x2+−0.000817808808.*x1.*x2.*x3+−23.6556137.*x1.^2 + 0.0316415509.*x1.^2.*x3+−0.00432064595.*x1.^2.*x2+−21704.0562.*1+−0.0894473145.*x1.^3
Predictive Eq. (3) Delta_SST = *f*(x1 = ISST_Mean, x2 = OHC, x3 = D26, x4 = MSLP)	IF OHC<=60 @(x1,x2,x3,x4) + 6.2042831.*x4 + 9.0400407.*x3 + 0.012021402.*x3.*x4+−34.469972.*x2 + 0.01463764.*x2.*x4+−0.057871413.*x2.*x3 + 8.7927954e-05.*x2.*x3.*x4 + 776.66701.*x1+ −0.49030434.*x1.*x4+−1.006713.*x1.*x3+−0.00052744652.*x1.*x3.*x4 + 2.0509349.*x1.*x2+ −0.00069208824.*x1.*x2.*x4+−0.0010858835.*x1.*x2.*x3+−19.438856.*x1.^2 + 0.0097900887.* x1.^2.*x4 + 0.027945368.*x1.^2.*x3+−0.02320013.*x1.^2.*x2+−9014.3284.*1 + 0.10729427.*x1.^3 IF OHC>60 @(x1,x2,x3,x4) + 34.6872402.*x4 + 43.933805.*x3+−0.0569728992.*x3.*x4+−76.0847299.*x2 + 0.0854220097.*x2.*x4+−0.0118381225.*x2.*x3 + 9.71790775e-06.*x2.*x3.*x4 + 2420.9874.*x1+ −2.49295821.*x1.*x4+−1.01715964.*x1.*x3 + 0.00193468257.*x1.*x3.*x4 + 2.31099936.*x1.*x2+ −0.00297248155.*x1.*x2.*x4 + 7.7402844e-05.*x1.*x2.*x3+−42.0192193.*x1.^2 + 0.044805495.* x1.^2.*x4+−0.0161696409.*x1.^2.*x3 + 0.0117037889.*x1.^2.*x2+−34067.955.*1+ −0.0358208116.*x1.^3
Predictive Eq. (4) Delta_SST = *f*(x1 = ISST_Mean, x2 = OHC, x3 = MSLP, x4 = LATITUDE)	IF OHC<=60 @(x1,x2,x3,x4) + -144.13751.*x4 + 0.68703036.*x3 + 0.037779468.*x3.*x4+−22.373939.*x2+ −0.12093889.*x2.*x4 + 0.029813403.*x2.*x3+−8.2211593e-05.*x2.*x3.*x4+−315.8087.*x1 + 9.2313392.*x1.*x4+−0.12627661.*x1.*x3+−0.0012802066.*x1.*x3.*x4 + 0.61541175.*x1.*x2 + 0.0073802028.*x1.*x2.*x4+−0.00096672748.*x1.*x2.*x3 + 8.6821285.*x1.^2+−0.14847711.*x1.^2. *x4 + 0.0035584695.*x1.^2.*x3 + 0.0029580054.*x1.^2.*x2 + 4283.3374.*1+−0.099571487.*x1.^3 IF OHC>60 @(x1,x2,x3,x4) + 171.140711.*x4 + 17.1398719.*x3+−0.172525557.*x3.*x4 + 38.8032938.*x2 + 0.11379356.*x2.*x4+−0.0184160248.*x2.*x3+−2.50374919e-05.*x2.*x3.*x4 + 930.635985.*x1+ −6.09274309.*x1.*x4+−0.996322858.*x1.*x3 + 0.00603582627.*x1.*x3.*x4+−2.10419091.*x1.*x2+ −0.00306892865.*x1.*x2.*x4 + 0.000649570396.*x1.*x2.*x3+−9.88263469.*x1.^2 + 0.00362720648.*x1.^2.*x4 + 0.0139252899.*x1.^2.*x3 + 0.0259228405.*x1.^2.*x2+ −16984.3976.*1+−0.0676851348.*x1.^3
Predictive Eq. (5) Delta_SST = *f*(x1 = ISST_Mean, x2 = MSLP, x3 = STORM SPEED, x4 = LATITUDE)	IF MSLP<=985 @(x1,x2,x3,x4) + -96.054973.*x4+−106.45553.*x3+−1.6203078.*x3.*x4+−8.0261865.*x2 + 0.10369266.*x2.*x4 + 0.12029066.*x2.*x3 + 0.00095905699.*x2.*x3.*x4+−517.24253.*x1 + 3.6874324.*x1.*x4 + 4.7956644.*x1.*x3 + 0.023267352.*x1.*x3.*x4 + 0.42137408.*x1.*x2+ −0.0038872664.*x1.*x2.*x4+−0.004864637.*x1.*x2.*x3 + 8.6510936.*x1.^2+−0.0025328032.*x1.^2.*x4+ −0.014077272.*x1.^2.*x3+−0.0047199674.*x1.^2.*x2 + 8672.9224.*1+−0.047872701.*x1.^3 IF MSLP>985 @(x1,x2,x3,x4) + 4.797035.*x4+−33.21866.*x3 + 0.6516741.*x3.*x4 + 2.6370376.*x2+ −0.0062376743.*x2.*x4 + 0.030516891.*x2.*x3+−0.0008628673.*x2.*x3.*x4 + 93.278365.*x1+ −0.28113806.*x1.*x4 + 1.0630202.*x1.*x3 + 0.007890786.*x1.*x3.*x4+−0.19574587.*x1.*x2 + 0.0004403575.*x1.*x2.*x4+−0.00068582489.*x1.*x2.*x3 + 0.089510573.*x1.^2+−0.0039567599.* x1.^2.*x4+−0.010236229.*x1.^2.*x3 + 0.003523817.*x1.^2.*x2+−1682.6955.*1+−0.041758772.*x1.^3

TABLE A3. (*Continued*)

Predictive Eq. (6)	IF OHC<=60
Delta_SST = *f*(x1 = ISST_Mean, x2 = OHC, x3 = STORM SPEED (m s^{-1}), x4 = LATITUDE)	@(x1,x2,x3,x4) + -14.467635.*x4 + 11.114666.*x3 + 0.63372575.*x3.*x4 + 15.64873.*x2+−0.11436561.*x2.*x4+−0.12573493.*x2.*x3+−0.00066736739.*x2.*x3.*x4+−138.88259.*x1 + 1.0045129.*x1.*x4+−1.3295993.*x1.*x3+−0.021430988.*x1.*x3.*x4+−0.98596346.*x1.*x2 + 0.0043226379.*x1.*x2.*x4 + 0.0050333354.*x1.*x2.*x3 + 5.1572958.*x1.^2+−0.017878399.*x1.^2.*x4 + 0.032227638.*x1.^2.*x3 + 0.015070256.*x1.^2.*x2 + 1253.7436.*1+−0.063782933.*x1.^3
	IF OHC>60
	@(x1,x2,x3,x4) + 34.856146.*x4 + 333.15038.*x3+−0.62939889.*x3.*x4 + 17.038097.*x2 + 0.022991348.*x2.*x4 + 0.22481598.*x2.*x3 + 0.00024598308.*x2.*x3.*x4+−982.46943.*x1+−2.2424263.*x1.*x4+−23.273575.*x1.*x3 + 0.020817622.*x1.*x3.*x4+−1.2284343.*x1.*x2+−0.00078499039.*x1.*x2.*x4+−0.0078207187.*x1.*x2.*x3 + 38.314327.*x1.^2 + 0.035850608.*x1.^2.*x4 + 0.4065797.*x1.^2.*x3 + 0.02207156.*x1.^2.*x2 + 8254.6753.*1+−0.49131583.*x1.^3
Shallow water predictive equation	IF MSLP< =985
Delta_SST = *f*(x1 = ISST_Mean, x2 = MSLP, x3 = STORM SPEED, x4 = LATITUDE)	@(x1,x2,x3,x4) + -131.5421.*x4+−172.08866.*x3 + 1.6604429.*x3.*x4+−7.2484883.*x2 + 0.085275219.*x2.*x4 + 0.12847129.*x2.*x3+−0.0013199021.*x2.*x3.*x4+−577.51434.*x1 + 6.0949846.*x1.*x4 + 6.3455442.*x1.*x3+−0.014061978.*x1.*x3.*x4 + 0.40105601.*x1.*x2+−0.0026925801.*x1.*x2.*x4+−0.0034152946.*x1.*x2.*x3 + 9.9885247.*x1.^2+−0.061937079.*x1.^2.*x4+−0.047166773.*x1.^2.*x3+−0.0053871052.*x1.^2.*x2 + 9306.165.*1+−0.033575095.*x1.^3
	IF MSLP>985
	@(x1,x2,x3,x4) + -23.821746.*x4+−25.056483.*x3+−0.88150189.*x3.*x4+−0.9974738.*x2 + 0.024960954.*x2.*x4 + 0.029439115.*x2.*x3 + 0.00077131981.*x2.*x3.*x4+−36.323473.*x1 + 0.86282889.*x1.*x4 + 1.9175549.*x1.*x3 + 0.0044008265.*x1.*x3.*x4 + 0.025630635.*x1.*x2+−0.00090645359.*x1.*x2.*x4+−0.0021689815.*x1.*x2.*x3 + 0.0091377491.*x1.^2+−0.00010554307.*x1.^2.*x4 + 0.0030133869.*x1.^2.*x3 + 0.00047900673.*x1.^2.*x2 + 1063.8643.*1+−0.0066518369.*x1.^3

REFERENCES

Balaguru, K., G. R. Foltz, L. R. Leung, S. M. Hagos, and D. R. Judi, 2018: On the use of ocean dynamic temperature for hurricane intensity forecasting. *Wea. Forecasting*, **33**, 411–418, https://doi.org/10.1175/WAF-D-17-0143.1.

——, and Coauthors, 2020: Characterizing tropical cyclones in the Energy Exascale Earth System Model version 1. *J. Adv. Model. Earth Syst.*, **12**, e2019MS002024, https://doi.org/10.1029/2019MS002024.

Boyd, J. D., 1987: Improved depth and temperature conversion equations for Sippican AXBTs. *J. Atmos. Oceanic Technol.*, **4**, 545–551, https://doi.org/10.1175/1520-0426(1987)004<0545:IDATCE>2.0.CO;2.

Chan, J. C. L., Y. Duan, and L. K. Shay, 2001: Tropical cyclone intensity change from a simple ocean–atmosphere coupled model. *J. Atmos. Sci.*, **58**, 154–172, https://doi.org/10.1175/1520-0469(2001)058<0154:TCICFA>2.0.CO;2.

Chen, S., J. A. Cummings, J. M. Schmidt, E. R. Sanabia, and S. R. Jayne, 2017: Targeted ocean sampling guidance for tropical cyclones. *J. Geophys. Res. Oceans*, **122**, 3505–3518, https://doi.org/10.1002/2017JC012727.

Cione, J. J., 2015: The relative roles of the ocean and atmosphere as revealed by buoy air–sea observations in hurricanes. *Mon. Wea. Rev.*, **143**, 904–913, https://doi.org/10.1175/MWR-D-13-00380.1.

——, and E. W. Uhlhorn, 2003: Sea surface temperature variability in hurricanes: Implications with respect to intensity change. *Mon. Wea. Rev.*, **131**, 1783–1796, https://doi.org/10.1175//2562.1.

——, P. G. Black, and S. H. Houston, 2000: Surface observations in the hurricane environment. *Mon. Wea. Rev.*, **128**, 1550–1561, https://doi.org/10.1175/1520-0493(2000)128<1550:SOITHE>2.0.CO;2.

——, E. A. Kalina, J. A. Zhang, and E. W. Uhlhorn, 2013: Observations of air–sea interaction and intensity change in hurricanes. *Mon. Wea. Rev.*, **141**, 2368–2382, https://doi.org/10.1175/MWR-D-12-00070.1.

Da, N. D., G. R. Foltz, and K. Balaguru, 2021: Observed global increases in tropical cyclone-induced ocean cooling and primary production. *Geophys. Res. Lett.*, **48**, e2021GL092574, https://doi.org/10.1029/2021GL092574.

Dare, R. A., and J. L. McBride, 2011: Sea surface temperature response to tropical cyclones. *Mon. Wea. Rev.*, **139**, 3798–3808, https://doi.org/10.1175/MWR-D-10-05019.1.

D'Asaro, E. A., T. B. Sanford, P. P. Niiler, and E. J. Terrill, 2007: Cold wake of Hurricane Frances. *Geophys. Res. Lett.*, **34**, L15609, https://doi.org/10.1029/2007GL030160.

Davis, C. A., 2018: Resolving tropical cyclone intensity in models. *Geophys. Res. Lett.*, **45**, 2082–2087, https://doi.org/10.1002/2017GL076966.

DeMaria, M., M. Mainelli, L. K. Shay, J. A. Knaff, and J. Kaplan, 2005: Further improvements in the Statistical Hurricane Intensity Prediction Scheme (SHIPS). *Wea. Forecasting*, **20**, 531–543, https://doi.org/10.1175/WAF862.1.

Demuth, J., M. DeMaria, and J. A. Knaff, 2006: Improvement of Advanced Microwave Sounder Unit tropical cyclone intensity and size estimation algorithms. *J. Appl. Meteor. Climatol.*, **45**, 1573–1581, https://doi.org/10.1175/JAM2429.1.

Domingues, R., and Coauthors, 2019: Ocean observations in support of studies and forecasts of tropical and extratropical cyclones. *Front. Mar. Sci.*, **6**, 446, https://doi.org/10.3389/fmars.2019.00446.

——, and Coauthors, 2021: Ocean conditions and the intensification of three major Atlantic hurricanes in 2017. *Mon. Wea.*

Rev., **149**, 1265–1286, https://doi.org/10.1175/MWR-D-20-0100.1.

Elsberry, R. L., T. S. Fraim, and R. N. Trapnell Jr., 1976: A mixed layer model of the oceanic thermal response to hurricanes. *J. Geophys. Res.*, **81**, 1153–1162, https://doi.org/10.1029/JC081i006p01153.

Emanuel, K. A., 1986: An air–sea interaction theory for tropical cyclones. Part I: Steady-state maintenance. *J. Atmos. Sci.*, **43**, 585–605, https://doi.org/10.1175/1520-0469(1986)043<0585:AASITF>2.0.CO;2.

Fisher, E. L., 1958: Hurricanes and the sea surface temperature field. *J. Atmos. Sci.*, **15**, 328–333, https://doi.org/10.1175/1520-0469(1958)015<0328:HATSST>2.0.CO;2.

Garcia, H. E., and Coauthors, 2019: World Ocean Atlas 2018: Product documentation. 20 pp., https://www.ncei.noaa.gov/sites/default/files/2020-04/woa18documentation.pdf.

Gilhousen, D. B., 1988: Quality control of meteorological data from automated marine stations. Preprints, *Fourth Int. Conf. on Interactive Information and Processing Systems for Meteorology, Oceanography, and Hydrology*, Miami, FL, Amer. Meteor. Soc., 113–117.

——, 1998: Improved real-time quality control of NDBC measurements. Preprints, *10th Symp. on Meteorological Observations and Instrumentation*, Phoenix, AZ, Amer. Meteor. Soc., 363–366.

Goni, G. J., and Coauthors, 2017: Autonomous and Lagrangian ocean observations for Atlantic tropical cyclone studies and forecasts. *Oceanography*, **30**, 92–103, https://doi.org/10.5670/oceanog.2017.227.

Hidaka, K., and Y. Akiba, 1955: Upwelling induced by a circular wind system. *Rec. Oceanogr. Works Japan*, **2**, 7–18.

Hlywiak, J., and D. S. Nolan, 2019: The influence of oceanic barrier layers on tropical cyclone intensity as determined through idealized, coupled numerical simulations. *J. Phys. Oceanogr.*, **49**, 1723–1745, https://doi.org/10.1175/JPO-D-18-0267.1.

Huang, B., C. Liu, V. Banzon, E. Freeman, G. Graham, B. Hankins, T. Smith, and H.-M. Zhang, 2021: Improvements of the Daily Optimum Interpolation Sea Surface Temperature (DOISST) version 2.1. *J. Climate*, **34**, 2923–2939, https://doi.org/10.1175/JCLI-D-20-0166.1.

Jacob, S. D., L. K. Shay, A. J. Mariano, and P. G. Black, 2000: The 3-D oceanic mixed-layer response to Hurricane Gilbert. *J. Phys. Oceanogr.*, **30**, 1407–1429, https://doi.org/10.1175/1520-0485(2000)030<1407:TOMLRT>2.0.CO;2.

Jaimes, B., and L. K. Shay, 2009: Mixed layer cooling in mesoscale oceanic eddies during Hurricanes Katrina and Rita. *Mon. Wea. Rev.*, **137**, 4188–4207, https://doi.org/10.1175/2009MWR2849.1.

——, and ——, 2010: Near-inertial wave wake of Hurricanes Katrina and Rita over mesoscale oceanic eddies. *J. Phys. Oceanogr.*, **40**, 1320–1337, https://doi.org/10.1175/2010JPO4309.1.

——, and ——, 2015: Enhanced wind-driven downwelling flow in warm oceanic eddy features during the intensification of Tropical Cyclone Isaac (2012): Observations and theory. *J. Phys. Oceanogr.*, **45**, 1667–1689, https://doi.org/10.1175/JPO-D-14-0176.1.

——, ——, and E. W. Uhlhorn, 2015: Enthalpy and momentum fluxes during hurricane Earl relative to underlying ocean features. *Mon. Wea. Rev.*, **143**, 111–131, https://doi.org/10.1175/MWR-D-13-00277.1.

Jaimes de la Cruz, B., L. K. Shay, J. B. Wadler, and J. E. Rudzin, 2021: On the hyperbolicity of the bulk air–sea heat flux functions: Insights into the efficiency of air–sea moisture disequilibrium for tropical cyclone intensification. *Mon. Wea. Rev.*, **149**, 1517–1534, https://doi.org/10.1175/MWR-D-20-0324.1.

Jayne, S. R., W. B. Owens, P. E. Robbins, A. K. Ekholm, N. M. Bogue, and E. R. Sanabia, 2022: The air-launched autonomous micro observer. *J. Atmos. Oceanic Technol.*, **39**, 491–502, https://doi.org/10.1175/JTECH-D-21-0046.1.

Landsea, C. W., and J. L. Franklin, 2013: Atlantic hurricane database uncertainty and presentation of a new database format. *Mon. Wea. Rev.*, **141**, 3576–3592, https://doi.org/10.1175/MWR-D-12-00254.1.

Le Hénaff, M., and Coauthors, 2021: The role of the Gulf of Mexico ocean conditions in the intensification of Hurricane Michael (2018). *J. Geophys. Res. Oceans*, **126**, e2020JC016969, https://doi.org/10.1029/2020JC016969.

Leipper, D. F., 1967: Observed ocean conditions and Hurricane Hilda, 1964. *J. Atmos. Sci.*, **24**, 182–186, https://doi.org/10.1175/1520-0469(1967)024<0182:OOCAHH>2.0.CO;2.

Leipper, D., and D. Volgenau, 1972: Hurricane heat potential of the Gulf of Mexico. *J. Phys. Oceanogr.*, **2**, 218–224, https://doi.org/10.1175/1520-0485(1972)002<0218:HHPOTG>2.0.CO;2.

Lin, I.-I., C.-H. Chen, I.-F. Pun, W. T. Liu, and C.-C. Wu, 2009: Warm ocean anomaly, air sea fluxes, and the rapid intensification of Tropical Cyclone Nargis (2008). *Geophys. Res. Lett.*, **36**, L03817, https://doi.org/10.1029/2008GL035815.

——, and Coauthors, 2013: An ocean cooling potential intensity index for tropical cyclones. *Geophys. Res. Lett.*, **40**, 1878–1882, https://doi.org/10.1002/grl.50091.

Lu, Z., G. Wang, and X. Shang, 2021: Inner-core sea surface cooling induced by a tropical cyclone. *J. Phys. Oceanogr.*, **51**, 3385–3400, https://doi.org/10.1175/JPO-D-21-0102.1.

Malkus, J. S., and H. Riehl, 1960: On the dynamics and energy transformations in steady-state hurricanes. *Tellus*, **12A** (1), 1–20, https://doi.org/10.3402/tellusa.v12i1.9351.

Mei, W., and C. Pasquero, 2013: Spatial and temporal characterization of sea surface temperature response to tropical cyclones. *J. Climate*, **26**, 3745–3765, https://doi.org/10.1175/JCLI-D-12-00125.1.

Meinig, C., and Coauthors, 2019: Public-private partnerships to advance regional ocean observing capabilities: A Saildrone and NOAA-PMEL case study and future considerations to expand to global scale observing. *Front. Mar. Sci.*, **6**, 448, https://doi.org/10.3389/fmars.2019.00448.

Meissner, T., F. J. Wentz, D. LeVine, and J. Scott, 2014: Aquarius salinity retrieval. Algorithm Theoretical Basis Doc., Addendum III, RSS Rep. 060414, 24 pp., https://images.remss.com/papers/rsstech/2014_Meissner_Aquarius_ATBD_Addendum3.pdf.

Meyers, P. C., L. K. Shay, and J. K. Brewster, 2014: Development and analysis of the systematically merged Atlantic regional temperature and salinity climatology for oceanic heat content estimates. *J. Atmos. Oceanic Technol.*, **31**, 131–149, https://doi.org/10.1175/JTECH-D-13-00100.1.

Miles, T. N., and Coauthors, 2021: Uncrewed ocean gliders and saildrones support hurricane forecasting and research. *Oceanography*, **34**, 78–81, https://doi.org/10.5670/oceanog.2021.supplement.02-28.

Mogensen, K. S., L. Magnusson, and J. R. Bidlot, 2017: Tropical cyclone sensitivity to ocean coupling in the ECMWF coupled model. *J. Geophys. Res. Oceans*, **122**, 4392–4412, https://doi.org/10.1002/2017JC012753.

Mrvalijevic, R. K., and Coauthors, 2013: Observations of the cold wake of Typhoon Fanapi (2010). *Geophys. Res. Lett.*, **40**, 316–321, https://doi.org/10.1029/2012GL054282.

Palmén, E., 1948: On the formation and structure of tropical hurricanes. *Geophysika*, **3**, 26–38.

Price, J. F., 1981: Upper ocean response to a hurricane. *J. Phys. Oceanogr.*, **11**, 153–175, https://doi.org/10.1175/1520-0485(1981)011<0153:UORTAH>2.0.CO;2.

——, 2009: Metrics of hurricane-ocean interaction: Vertically-integrated or vertically-averaged ocean temperature? *Ocean Sci.*, **5**, 351–368, https://doi.org/10.5194/os-5-351-2009.

——, T. B. Sanford, and G. Z. Forristall, 1994: Forced stage response to a moving hurricane. *J. Phys. Oceanogr.*, **24**, 233–260, https://doi.org/10.1175/1520-0485(1994)024<0233:FSRTAM>2.0.CO;2.

Reul, N., Y. Quilfen, B. Chapron, S. Fournier, V. Kudryavtsev, and R. Sabia, 2014: Multisensor observations of the Amazon-Orinoco River plume interactions with hurricanes. *J. Geophys. Res. Oceans*, **119**, 8271–8295, https://doi.org/10.1002/2014JC010107.

Reynolds, R. W., T. M. Smith, C. Liu, D. B. Chelton, K. S. Casey, and M. G. Schlax, 2007: Daily high-resolution blended analyses for sea surface temperature. *J. Climate*, **20**, 5473–5496, https://doi.org/10.1175/2007JCLI1824.1.

Rudzin, J. E., L. K. Shay, B. Jaimes, and J. K. Brewster, 2017: Upper ocean observations in eastern Caribbean Sea reveal barrier layer within a warm core eddy. *J. Geophys. Res. Oceans*, **122**, 1057–1071, https://doi.org/10.1002/2016JC012339.

——, ——, and W. E. Johns, 2018: The influence of the barrier layer on SST response during tropical cyclone wind forcing using idealized experiments. *J. Phys. Oceanogr.*, **48**, 1471–1478, https://doi.org/10.1175/JPO-D-17-0279.1.

——, ——, and B. Jaimes de la Cruz, 2019: The impact of the Amazon–Orinoco River plume on enthalpy flux and air–sea interaction within Caribbean Sea tropical cyclones. *Mon. Wea. Rev.*, **147**, 931–950, https://doi.org/10.1175/MWR-D-18-0295.1.

Sanabia, E. R., and S. R. Jayne, 2020: Ocean observations under two major hurricanes: Evolution of the response across the storm wakes. *AGU Adv.*, **1**, e2019AV000161, https://doi.org/10.1029/2019AV000161.

Sanford, T. B., J. F. Price, J. B. Girton, and D. C. Webb, 2007: Highly resolved observations and simulations of the ocean response to a hurricane. *Geophys. Res. Lett.*, **34**, L13604, https://doi.org/10.1029/2007GL029679.

——, ——, and ——, 2011: Upper-ocean response to Hurricane Frances (2004) observed by profiling EM-APEX floats. *J. Phys. Oceanogr.*, **41**, 1041–1056, https://doi.org/10.1175/2010JPO4313.1.

Shay, L. K., and E. Uhlhorn, 2008: Loop Current response to Hurricanes Isidore and Lili. *Mon. Wea. Rev.*, **136**, 3248–3274, https://doi.org/10.1175/2007MWR2169.1.

——, P. G. Black, A. J. Mariano, J. D. Hawkins, and R. L. Elsberry, 1992: Upper ocean response to Hurricane Gilbert. *J. Geophys. Res.*, **97**, 20 227–20 248, https://doi.org/10.1029/92JC01586.

——, A. J. Mariano, S. D. Jacob, and E. H. Ryan, 1998: Mean and near-inertial ocean current response to Hurricane Gilbert. *J. Phys. Oceanogr.*, **28**, 858–889, https://doi.org/10.1175/1520-0485(1998)028<0858:MANIOC>2.0.CO;2.

——, G. J. Goni, and P. G. Black, 2000: Effects of a warm oceanic feature on Hurricane Opal. *Mon. Wea. Rev.*, **128**, 1366–1383, https://doi.org/10.1175/1520-0493(2000)128<1366:EOAWOF>2.0.CO;2.

——, and Coauthors, 2011: Airborne ocean surveys of the Loop Current complex from NOAA WP-3D in support of the Deep Water Horizon oil spill. *Monitoring and Modeling the Deepwater Horizon Oil Spill: A Record-Breaking Enterprise*, *Geophys. Monogr.*, Vol. 195, Amer. Geophys. Union, 131–151.

——, J. Brewster, E. Maturi, D. Donahue, P. Meyers, and C. McCaskill, 2019a: Satellite products and service review board: Algorithm Theoretical Basis Document: Satellite-derived oceanic heat content product, version 3.2. NOAA/RSMAS, 49 pp., https://www.ospo.noaa.gov/Products/ocean/assets/ATBD_OHC_NESDIS_V3.2.pdf.

——, ——, B. Jaimes, C. Gordon, K. Fennel, P. Furze, H. Fargher, and R. He, 2019b: Physical and biochemical structure measured by APEX-EM floats. *2019 IEEE/OES Twelfth Current, Waves and Turbulence Measurement (CWTM)*, San Diego, CA, Institute of Electrical and Electronics Engineers, 1–6, https://doi.org/10.1109/CWTM43797.2019.8955168.

Suda, K., 1943: *The Science of the Sea (Kaiyō Kagaku)*. Kokin Shoin, 284 pp.

Testor, P., and Coauthors, 2019: OceanGliders: A component of the integrated GOOS. *Front. Mar. Sci.*, **6**, 422, https://doi.org/10.3389/fmars.2019.00422.

Wadler, J. B., J. A. Zhang, B. Jaimes, and L. K. Shay, 2018: Downdrafts and the evolution of boundary layer thermodynamics in Hurricane Earl (2010) before and during rapid intensification. *Mon. Wea. Rev.*, **146**, 3545–3565, https://doi.org/10.1175/MWR-D-18-0090.1.

——, J. J. Cione, J. A. Zhang, E. A. Kalina, and J. Kaplan, 2022: The effects of environmental wind shear direction on tropical cyclone boundary layer thermodynamics and intensity change from multiple observational datasets. *Mon. Wea. Rev.*, **150**, 115–134, https://doi.org/10.1175/MWR-D-21-0022.1.

Wang, X., G. Han, Y. Qi, and W. Li, 2011: Impact of barrier layer on typhoon-induced sea surface cooling. *Dyn. Atmos. Oceans*, **52**, 367–385, https://doi.org/10.1016/j.dynatmoce.2011.05.002.

Zhang, J. A., P. G. Black, J. R. French, and W. M. Drennan, 2008: First direct measurements of enthalpy flux in the hurricane boundary layer: The CBLAST results. *Geophys. Res. Lett.*, **35**, L14813, https://doi.org/10.1029/2008GL034374.

——, J. J. Cione, E. A. Kalina, E. W. Uhlhorn, T. Hock, and J. A. Smith, 2017: Observations of infrared sea surface temperature and air-sea interaction in Hurricane Edouard (2014) using GPS dropsondes. *J. Atmos. Oceanic Technol.*, **34**, 1333–1349, https://doi.org/10.1175/JTECH-D-16-0211.1.

Zweng, M. M., and Coauthors, 2018: *Salinity*. Vol. 2, *World Ocean Atlas 2018*, NOAA Atlas NESDIS 82, 50 pp., https://www.ncei.noaa.gov/sites/default/files/2022-06/woa18_vol2.pdf.